Numerical study of time-dependent deformation and cracking in brittle rocks with phase-field method and application to slope instability analysis

Meng Wang, Zhan Yu, Wanqing Shen, Jianfu Shao

Numerical study of time-dependent deformation and cracking in brittle rocks with phase-field method and application to slope instability analysis

Meng WANG[a,b], Zhan YU[b], Wanqing SHEN[b], Jianfu SHAO[a,b,*]

[a] *Key Laboratory of Ministry of Education for Geomechanics and Embankment Engineering, Hohai University, Nanjing, 210098 China*
[b] *Univ. Lille, CNRS, Centrale Lille, UMR 9013 - LaMcube, F-59000 Lille, France*

Abstract

Most rocks exhibit time-dependent deformation and failure. Two main mechanisms are generally considered, the progressive growth of cracks and viscoelastic and/or viscoplastic deformation. In this study, cracking process is described by a viscous phase-field method which is coupled with a viscoplastic model. The evolution of crack field is controlled by both elastic and viscoplastic tensile volumetric and deviatoric strains. The threshold of viscoplastic deformation is weakened by the growth of cracks. The efficiency of the proposed model is first assessed by comparing numerical predictions with experimental data in triaxial compression and creep tests. Then, the proposed model is applied to modeling time-dependent deformation and failure process of a high slope section in the left bank of Jinping-I hydropower station in China. Numerical predictions are compared with field measurements.

Keywords: Damage, Cracking, viscoplastic deformation, Brittle rocks Phase-field method, Slope instability

1. Introduction

Damage due to initiation and propagation of cracks is commonly observed in brittle rocks. Macroscopic failure of these materials is generally driven by the transition from micro-cracks

*Corresponding author
Email address: jian-fu.shao@polytech-lille.fr (Jianfu SHAO)

to macro-cracks or fractures [1, 2]. Further, the so-called sub-critical slow propagation of micro-cracks and their coalescence [3, 4] can lead to time-dependent deformation and failure. Different types of experimental studies have been reported. For instance, in the framework of linear fracture mechanics, double torsion tests were performed to identify the sub-critical growth kinetics of cracks in various rocks [5, 6, 7, 8].

On the other hand, most rocks also exhibits viscoelastic and viscoplastic deformation under different stress states and environmental conditions [9, 10, 11, 12, 13]. According to previous studies [10, 14], the irrecoverable viscoplastic deformation should be the main responsible for the time-dependent delayed failure of rock engineering structures. Moreover, in many rocks, the viscoplastic deformation is intimately coupled with the growth of cracks. The macroscopic plastic and viscoplastic deformation can be partially related to the frictional sliding along micro-crack surfaces [15, 16, 17]. The viscoplastic deformation can be enhanced by the induced growth of cracks while the cracking process is affected by the creep deformation of materials. Therefore, it is primordial to take into account such a coupling phenomenon between cracking and viscoplastic deformation.

From the point of view of engineering application, instability and failure of engineered rock structures and natural systems can also be caused by time-dependent crack growth and viscoplastic deformation. For instance, many catastrophic landslides were induced by the accumulation of creep deformation and slow crack propagation and localization [18, 19]. Before the final failure, a gradual increase of deformation over time was monitored in a number of typical landslides [20, 21]. For instance, landslide of a natural slope caused by tunnel excavation was reported in [22]. In that accident, the slope failure occurred a few days after an arriving entrance of the tunnel was cut through. Progressive failure was clearly observed while no evidence of rainfall or underground water movement could be monitored [23]. Some experimental investigations were performed to understand the physical mechanisms involved in rainfall induced landslides [24, 25]. In many cases, natural hazards should be analyzed as evolutionary processes by taking into account time-dependent mechanical behavior of geological formations [26], in particular creep deformation and slow growth of cracks. The widely used limit equilibrium methods mainly focused on ultimate

instability mechanisms and do not considered progressive failure processes involved.

In order to complete the limit analysis methods and provide a finer description of natural hazards, different types of numerical methods have been developed. Briefly, two families of methods are available. In the first family, continuum mechanics based approaches are developed by using suitable constitutive models. Some of them were applied to analyzing progressive deformation and stability of rainfall-induced landslides [27, 28, 29, 30]. Viscoelastic and viscoplastic models were widely used to describe the time-dependent deformation of rocks and soils. For instance, the extended finite element method (XFEM) was used in [31, 32]. The mechanical response of materials has been studied by incorporating basis functions extracted from viscoelastic asymptotic fields. However, special treatments are necessary in simulating the complex crack topology, branching and multi-cracks configurations [33]. In the second family, one can find various types of discrete methods considering rock formations as an assembly of particles and blocks [34]. In particular, the discrete element model (DEM) has been employed to study the creep behavior of rocks, such as in [35, 36]. Fractures are created when the bonds between particles or blocks are broken, resulting that fracturing paths are not arbitrary but depend on the initial arrangement of particles and blocks [37].

During the recent years, the so-called phase-method has attracted more and more interest in view of cracking modeling in various engineering fields including geological materials [38]. Inspired by the variational principle for linear fracture mechanics [39], this method was initially formulated for studying brittle fractures in elastic materials [40, 41]. Based on approximation methods of functions with jumps [42, 43, 44], the evolution of sharp crack surface area is approximated by that of a regularized crack surface density function, which depends on an auxiliary phase-field (damage) variable and its gradient. Consequently, the phase-field method provides a non-local approach to describe the continuous transition from diffuse damage (micro-cracks) to macro-cracks in the form of localized damage bands. Furthermore, the phase-field method is particularly suitable to deal with merging and branching of multiple cracks with no additional effort or heuristics [45]. For geological materials under compressive stresses, particular efforts were made on the description of shear and mixed

cracks [46, 47, 48], and for coupled thermo-hydromechanical problems [49, 50, 51]. Moreover, the application of phase-field method has also been extended from fractures in solids with infinitesimal strains to plates, shells and composites under finite strains [52]. In view of the dynamic cracking analysis, explicit phase field models were also reported [53]. In addition, a deep neural network (DNN) based solution for solving phase-field fracture was proposed by [54], which totally avoids a classical discretization to solve the underlying coupled partial differential equations. Despite all these advances, only few studies have been devoted to time-dependent fracturing in viscoplastic rocks [55]. However, as the main limitation of phase-field method, the propagation of sharp cracks is approximated by the growth of damage field and onset of localized damage bands. Consequently, the time-dependent cracking process is described by the time-dependent evolution of damage field coupled with the viscoplastic flow.

In the present work, we shall develop an efficient numerical modeling method of progressive cracking process in rocks exhibiting an elastic-viscoplastic behavior. The initiation and propagation of cracks is described by a time-dependent phase field method while the creep deformation of rocks by a viscoplastic model. The growth of phase field is affected by the viscoplastic deformation and inversely the threshold of viscoplastic flow is degraded by the induced cracks. The proposed numerical method is implemented in a standard finite element framework. Its efficiency is assessed through comparisons with both laboratory tests and field observations.

2. Time-dependent phase-field model for viscoplastic rocks

2.1. Regularized crack surface description

Let $\Omega \subset \mathbb{R}$ be a volumetric domain of solid material with an external boundary $\partial\Omega$, which contains a number of cracks $\Gamma_i, i = 1, ..N$. It is generally very delicate to trace the evolution of each individual crack during loading history. In order to overcome such difficulty, a regularized description of cracks has been introduced in the so-called phase-field method [40, 45, 56, 57]. The exact description of discontinuous sharp cracks is approximated

by a continuous volumetric distribution of crack surface density. More precisely, the total area of sharp crack surfaces A_Γ is approximated a regularized quantity A_{Γ_d} as follows:

$$A_\Gamma = \sum_{i=1}^{N} A_{\Gamma_i} \cong A_{\Gamma_d} = \int_\Omega \Gamma_d(d, \nabla d) \mathrm{d}V \tag{1}$$

The function $\Gamma_d(d, \nabla d)$ denotes the crack surface area per unit initial volume ($\mathrm{m}^2/\mathrm{m}^3$). The auxiliary scalar variable $d(\mathbf{x}) \in [0, 1]$ defines an undamaged state by 0 and a fully damaged state by 1. It is usually called phase-field variable and physically equivalent to that used in continuum damage mechanics. It is noticed that the crack density function $\Gamma_d(d, \nabla d)$ is not only dependent on the local damage variable d but also on its gradient ∇d. Therefore, the crack density is a non-local function of damage variable. This is an essential feature allowing the regularization of damage localization process and avoiding the related pathological mesh dependency. Among various choices for the crack surface density function, the following widely used form introduced in [43] is adopted here:

$$\Gamma_d(d, \nabla d) = \frac{d^2}{2l_d} + \frac{l_d}{2}|\nabla d|^2 \tag{2}$$

The parameter $l_d > 0$ is a length scale which defines the width of smeared cracks represented by localized damage zones. Further, the cracking is an irreversible process. The evolution rate of crack surface area should be not negative and it is usually defined as follows:

$$\dot{A}_{\Gamma_d} = \frac{\mathrm{d}}{\mathrm{d}t} \int_\Omega \Gamma_d(d, \nabla d) \mathrm{d}V = \int_\Omega \dot{\Gamma}_d \mathrm{d}V \geq 0 \tag{3}$$

with:

$$\dot{\Gamma}_d = (\frac{d}{l_d})\dot{d} + l_d \nabla d \cdot \nabla \dot{d} \geq 0 \tag{4}$$

2.2. Energy functional

In this study, we consider an isotropic rock material exhibiting an elastic-viscoplastic behavior and the transition from diffuse damage to localized cracking which is described by the phase-field method. With the assumption of small strains, the total strain tensor $\boldsymbol{\varepsilon}$ is conventionally divided into an elastic part $\boldsymbol{\varepsilon}^e$ and a viscoplastic part $\boldsymbol{\varepsilon}^{vp}$ such as $\boldsymbol{\varepsilon} = \boldsymbol{\varepsilon}^e + \boldsymbol{\varepsilon}^{vp}$. The total energy functional can be expressed in the following general form:

$$E(\boldsymbol{\varepsilon}^e, \boldsymbol{\varepsilon}^{vp}, d) = \int_\Omega \left[w^e(\boldsymbol{\varepsilon}^e, d) + w^{vp}(\boldsymbol{\varepsilon}^{vp}, d) \right] \mathrm{d}v + E^{crack} \tag{5}$$

w^e is the elastic strain energy density per initial unit volume of damaged material. w^{vp} denotes the viscoplastic strain energy density (dissipated and stored). The third term E^{crack} represents the energy needed to create cracks in Ω.

2.2.1. Elastic strain energy

The elastic strain energy of material is affected by cracking process and it is a function of the damage variable d. Inversely, the damage evolution is driven by the growth of elastic strain energy. In this work, it is assumed that the damage evolution is motivated only the tensile (positive) volumetric strain and deviatoric (or shear) strains. For this purpose, the elastic strain energy of undamaged material is conveniently decomposed as follows:

$$\begin{cases} w_0^e(\boldsymbol{\varepsilon}^e) = w_{0-}^e(\boldsymbol{\varepsilon}^e) + w_{0+}^e(\boldsymbol{\varepsilon}^e) \\ w_{0-}^e = \dfrac{k_0}{2}[\langle \mathrm{tr}(\boldsymbol{\varepsilon}^e)\rangle_-]^2 \qquad\qquad , \boldsymbol{\varepsilon}_{dev}^e = \boldsymbol{\varepsilon}^e - \dfrac{\mathrm{tr}(\boldsymbol{\varepsilon}^e)}{3}\boldsymbol{I} \\ w_{0+}^e = \dfrac{k_0}{2}[\langle \mathrm{tr}(\boldsymbol{\varepsilon}^e)\rangle_+]^2 + \mu_0 \boldsymbol{\varepsilon}_{dev}^e : \boldsymbol{\varepsilon}_{dev}^e \end{cases} \tag{6}$$

k_0 and μ_0 are respectively the elastic bulk and shear modulus of undamaged material. $\langle x\rangle_+ = x$ if $x > 0$ and $\langle x\rangle_+ = 0$ if $x \leq 0$, inversely for $\langle x\rangle_-$. $\boldsymbol{I}$ is the second-order identity tensor. Accordingly, the elastic strain density function of damaged material is written as:

$$w^e(\boldsymbol{\varepsilon}^e, d) = w_{0-}^e(\boldsymbol{\varepsilon}^e) + g(d) w_{0+}^e(\boldsymbol{\varepsilon}^e, d) \tag{7}$$

The so-called degradation function $g(d)$ defines the coupling between the elastic strain energy and damage evolution. The elastic stress-strain relations of damaged material are obtained from the standard derivation of w^e:

$$\boldsymbol{\sigma} = \frac{\partial w^e}{\partial \boldsymbol{\varepsilon}^e} = \mathbb{C}(d) : \boldsymbol{\varepsilon}^e \tag{8}$$

$\boldsymbol{\sigma}$ is Cauchy stress tensor. $\mathbb{C}(d)$ denotes the elastic stiffness tensor of damaged material and it is here given by:

$$\mathbb{C}(d) = r_e^- k_0 \boldsymbol{I} \otimes \boldsymbol{I} + g(d)[r_e^+ k_0 \boldsymbol{I} \otimes \boldsymbol{I} + 2\mu_0(\mathbb{I} - \frac{1}{3}\boldsymbol{I} \otimes \boldsymbol{I})] \tag{9}$$

$\mathbb{I}$ is the fourth-order symmetric identity tensor. The coefficients $r_e^{\pm} = \frac{1}{2}\{\mathrm{sign}[\pm \mathrm{tr}(\boldsymbol{\varepsilon}^e)] + 1\}$ describe the fact that the bulk modulus k is affected by open cracks ($r_e^+ = 1$ and r_e^-=0) but not affected by closed shear cracks ($r_e^+ = 0$ and r_e^-=1).

It is noticed that the choice of $g(d)$ leads to different types of elastic properties degradation. A review on the choice of degradation function and its consequences can be found in [58]. Among various forms of $g(d)$ proposed in previous studies [40, 57, 49], the most widely used one is $g(d) = (1-d)^2$ by satisfying the condition $g'(d=1) = 0$. It is adopted in this study.

2.2.2. Viscoplastic strain energy

Furthermore, since the concept of elasto-viscoplasticity was firstly introduced by [59], the elasto-viscoplastic behavior of rocks has been widely discussed and some significant progresses have been reported in [60, 11]. Moreover, An elasto-viscoplastic model based on Perzyna's general theory was proved to be in good agreement with both laboratory and in situ data by [61]. Consequently, the classical Perzyna's formulation [59, 62] will be coupled with the phase-field method to describe the time-dependent behavior of brittle rocks in this paper.

Time-dependent deformation of rocks can be related to various mechanisms such as viscoplastic flow, sub-critical growth of micro-cracks etc. In this work, for the sake of simplicity, it is assumed that the time-dependent deformation and cracking is mainly driven by the viscoplastic flow. Further, by putting the emphasis on cracking modeling by the phase-field method, the viscoplastic deformation is described by using the classical Perzyna's formulation [59, 62] and a simple constitutive model.

The accumulated viscoplastic strain $\boldsymbol{\varepsilon}^{vp}$ is calculated by time integration of its flow rate $\dot{\boldsymbol{\varepsilon}}^{vp}$:

$$\boldsymbol{\varepsilon}^{vp}(t) = \int_0^t \dot{\boldsymbol{\varepsilon}}^{vp}(\tau)\mathrm{d}\tau \tag{10}$$

The viscoplastic strain rate is defined by the following widely used exponential form:

$$\dot{\boldsymbol{\varepsilon}}^{vp} = \eta\langle f^{vp}(\boldsymbol{\sigma})\rangle_+^n \dot{\lambda}\frac{\partial G^{vp}}{\partial \boldsymbol{\sigma}} \tag{11}$$

η is a viscosity parameter controlling the initial rate of viscoplastic flow. $\langle\rangle_+$ are the Macaulay brackets. f^{vp} represents the viscoplastic loading function. Similarly to some previous studies [63], it is assumed that the viscoplastic flow of rocks can be enhanced by the induced damage.

Therefore, the following damage-coupled form is adopted [64]:

$$f^{vp}(\boldsymbol{\sigma}) = \frac{q - g_{vp}(d)\sigma_s}{p_r} \tag{12}$$

$q = \sqrt{3\boldsymbol{s} : \boldsymbol{s}/2}$ is the conventional generalized deviatoric stress, with $\boldsymbol{s} = \boldsymbol{\sigma} - \frac{\mathrm{tr}(\boldsymbol{\sigma})}{3}\boldsymbol{I}$ being the deviatoric stress tensor. The parameter σ_s denotes the initial threshold for viscoplastic flow and p_r =1 MPa is a fixed normalizing stress. $g_{vp}(d)$ is the degradation function for viscoplastic flow. The use of product form in $g_{vp}(d)\sigma_s$ means that the viscoplastic threshold is progressively reduced by the growth of damage. For the sake of simplicity, the same form as the elastic degradation function is here used: $g_{vp}(d) = g(d)$.

The coefficient $\dot{\lambda}$ defines the current amplitude of the viscoplastic strain rate, which is a function of the accumulated viscoplastic strain:

$$\dot{\lambda} = (1 - \varepsilon_{vp}^{eq})^m \text{ , with } \varepsilon_{vp}^{eq} = \int_0^t \sqrt{\frac{2}{3}\dot{\boldsymbol{\varepsilon}}_{dev}^{vp}(\tau) : \dot{\boldsymbol{\varepsilon}}_{dev}^{vp}(\tau)}\mathrm{d}\tau \tag{13}$$

in which $\dot{\boldsymbol{\varepsilon}}_{dev}^{vp} = \dot{\boldsymbol{\varepsilon}}^{vp} - \frac{\mathrm{tr}(\dot{\boldsymbol{\varepsilon}}^{vp})}{3}\boldsymbol{I}$ is the viscoplastic deviatoric strain tensor. n and m are two material parameters.

In the viscoplastic flow rule (11), the scalar-valued function G^{vp} is a potential which defines the components of viscoplastic strain rate. Different forms are available in literature. For hard rocks, it was widely assumed that the viscoplastic flow produced the time-dependent deviatoric strains only. Therefore, a very simply viscoplastic flow potential $G^{vp} = q$ was used in some previous studies [65, 64]. However, according to laboratory creep tests on Jinping marble diabase [13], large volumetric creep strain was also obtained. For this reason, the following viscoplastic flow potential is proposed in this work:

$$G^{vp} = q + c_v p \tag{14}$$

where $p = \mathrm{tr}(\boldsymbol{\sigma})/3$ is the mean stress. The parameter c_v defines the volumetric viscoplastic strain rate.

In consistency with the elastic strain energy decomposition (6), the viscoplastic strain energy of undamaged material is also decomposed into two parts: respectively coupled

and not with the induced damage d. Therefore, the viscoplastic strain energy of damaged materials is given by:

$$\begin{cases} w^{vp}(\boldsymbol{\varepsilon}^{vp}, d) = w^{vp}_{0-}(\boldsymbol{\varepsilon}^{vp}) + g(d) w^{vp}_{0+}(\boldsymbol{\varepsilon}^{vp}) \\ w^{vp}_{0-} = \displaystyle\int_0^t \boldsymbol{\sigma}(\tau) : \dot{\boldsymbol{\varepsilon}}^{vp}_{sph-}(\tau) \mathrm{d}\tau \\ w^{vp}_{0+} = \displaystyle\int_0^t \boldsymbol{\sigma}(\tau) : [\dot{\boldsymbol{\varepsilon}}^{vp}_{sph+}(\tau) + \dot{\boldsymbol{\varepsilon}}^{vp}_{dev}(\tau)] \mathrm{d}\tau \end{cases}, \quad \begin{cases} \dot{\boldsymbol{\varepsilon}}^{vp}_{sph-} = \dfrac{\langle \mathrm{tr}(\dot{\boldsymbol{\varepsilon}}^{vp}) \rangle_-}{3} \boldsymbol{I} \\ \dot{\boldsymbol{\varepsilon}}^{vp}_{sph+} = \dfrac{\langle \mathrm{tr}(\dot{\boldsymbol{\varepsilon}}^{vp}) \rangle_+}{3} \boldsymbol{I} \\ \dot{\boldsymbol{\varepsilon}}^{vp}_{dev} = \dot{\boldsymbol{\varepsilon}}^{vp} - \dfrac{\mathrm{tr}(\dot{\boldsymbol{\varepsilon}}^{vp})}{3} \boldsymbol{I} \end{cases} \tag{15}$$

2.2.3. Crack growth related energy

In the variational framework for fracture mechanics, the crack growth or the evolution of damage variable is seen as an energy minimization problem [39, 66]. As in previous studies [67, 57], the energy related to fracture growth is here assumed to be fully dissipated. Moreover, the classical Griffith-type critical energy release rate is here adopted to quantify the work needed for an instantaneous crack surface creation [68]. Therefore, using the crack surface density defined in (2), the total energy dissipated in instantaneous crack creation can be expressed as follows:

$$E^{crack-ins} = \int_\Omega g_c \Gamma_d \mathrm{d}V \tag{16}$$

The parameter g_c denotes the energy needed for the creation of unit crack surface in unit initial volume (N/m). By assuming that the value of g_c is time-independent, the crack energy dissipation rate can be calculated as:

$$\dot{E}^{crack-ins} = \int_\Omega g_c \dot{\Gamma}_d \mathrm{d}V = \int_\Omega g_c \big[\big(\frac{d}{l_d}\big) \dot{d} + l_d \nabla d \cdot \nabla \dot{d} \big] \mathrm{d}V \tag{17}$$

In some situations, it is important to take into account a time-dependent or rate-dependent growth of cracks. Therefore, we shall also quantify the energy needed for such a crack growth process. Based on previous studies [69, 70], the following specific form is adopted:

$$\dot{E}^{crack-vis} = \int_\Omega \eta_d \dot{d}^2 \mathrm{d}V \tag{18}$$

in which $\eta_d \geq 0$ ($N.s/m^2$) is a viscosity parameter. Accordingly, the total dissipation rate crack growth is given by:

$$\dot{E} = \dot{E}^{crack-ins} + \dot{E}^{crack-vis} \tag{19}$$

2.3. Governing equations

The mechanical boundary values problem with crack growth (or phase-field evolution) can be solved by the minimization of the following potential function:

$$\dot{\Pi}(\dot{\boldsymbol{u}}, \dot{d}) = \dot{E}(\dot{\boldsymbol{u}}, \dot{d}) - \dot{P}(\dot{\boldsymbol{u}}) = 0 \tag{20}$$

By using the elastic strain energy, viscoplastic strain energy and crack growth energy defined above, the rate of the total energy functional $\dot{E}$ is given by:

$$\begin{aligned} \dot{E}(\dot{\boldsymbol{\varepsilon}}^e, \dot{\boldsymbol{\varepsilon}}^{vp}, \dot{d}) = \int_\Omega \dot{w}^e + \dot{w}^{vp} \, \mathrm{d}V = \int_\Omega \big[\frac{\partial (w^e + w^{vp})}{\partial d}\dot{d} + \boldsymbol{\sigma} : (\dot{\boldsymbol{\varepsilon}}^e + \dot{\boldsymbol{\varepsilon}}^{vp})\big]\mathrm{d}V \\ + \int_\Omega \{g_c\big[(\frac{d}{l_d})\dot{d} + l_d \nabla d \cdot \nabla \dot{d}\big] + \eta_d \dot{d}^2\}\mathrm{d}V \end{aligned} \tag{21}$$

As the evolution of phase-field variable d is driven by elastic and viscoplastic strains (or equivalently by dis displacement field $\boldsymbol{u}$) [40, 56], the external applied work rate is simply expressed as:

$$\dot{P} = \int_\Omega \boldsymbol{b} \cdot \dot{\boldsymbol{u}} \mathrm{d}V + \int_{\partial\Omega_t} \boldsymbol{t} \cdot \dot{\boldsymbol{u}} \mathrm{d}A \tag{22}$$

where $\boldsymbol{b}$ is a given body force field per unit volume (N/m^3) and $\boldsymbol{t}$ a prescribed surface traction (N/m^2) on the external boundary $\partial\Omega_t$.

The energy balance condition $\dot{\Pi} = 0$ leads to the following integral equation:

$$\begin{aligned} &\int_\Omega -\big[\mathrm{div}(\boldsymbol{\sigma}) + \boldsymbol{b}\big] \cdot \dot{\boldsymbol{u}} \mathrm{d}V + \int_{\partial\Omega} \big[\boldsymbol{\sigma} \cdot \boldsymbol{n} - \boldsymbol{t}\big] \cdot \dot{\boldsymbol{u}} \mathrm{d}A \\ &+ \int_\Omega \big[\frac{\partial (w^e + w^{vp})}{\partial d} + \frac{g_c}{l_d} d - g_c l_d \Delta d + \eta_d \dot{d}\big] \cdot \dot{d} \mathrm{d}V + \int_{\partial\Omega} \big[g_c l_d \nabla d \cdot \boldsymbol{n}\big] \cdot \dot{d} \mathrm{d}A = 0, \quad \forall \Omega \end{aligned} \tag{23}$$

in which $\Delta d = \mathrm{div}(\nabla d)$. Accordingly, one gets easily the following local governing equations for the mechanical (or displacement) problem:

$$\mathrm{div}(\boldsymbol{\sigma}(t)) + \boldsymbol{b} = 0 \text{ , with } \boldsymbol{\sigma}(t) = \mathbb{C}(d) : \big[\boldsymbol{\varepsilon} - \boldsymbol{\varepsilon}^{vp}(t)\big] \tag{24}$$

It is worth noticing that as the viscoplastic strains evolve with time, the current stress tensor is also a function of time. However, for the sake of simplicity, it is assumed that the time-dependent progressive deformation and cracking in rock structures can be seen as a

quasi-static process. Therefore, the inertia terms are not taken into account in the balance equations. The governing equation for the phase-field evolution is given by:

$$\eta_d \dot{d} = 2(1-d)(w_{0+}^e + w_{0+}^{vp}) - g_c\big[\frac{d}{l_d} - l_d \Delta d\big] \tag{25}$$

In order to verify the irreversible condition of crack growth $\dot{\Gamma}_d \geq 0$ and $\dot{d} \geq 0$, the concept of energy history functional introduced in [40] is here adopted and expressed by:

$$\mathcal{H}(t) = \max_{\tau \in [0,t]} [w_{0+}^e(\tau) + w_{0+}^{vp}(\tau)] \tag{26}$$

Consequently, the governing equation of phase-field evolution problem is rewritten as follows:

$$\eta_d \dot{d} = 2(1-d)\mathcal{H} - g_c\big[\frac{d}{l_d} - l_d \Delta d\big] \tag{27}$$

3. Numerical implementation in finite element framework

The time-dependent phase-field evolution is coupled with the displacement (stress) field solution. Both problems are here solved by using the classical finite element method. The main steps of numerical implementation are outlined in this section.

3.1. Weak forms

In view of finite element discretization, the governing equations (24) and (27) are transformed into the corresponding weak forms by using the standard Galerkin procedure with the test functions $\delta \boldsymbol{u}$ and δd respectively. For instance, one gets the weak form integral for the displacement problem as:

$$\int_\Omega \boldsymbol{\sigma} : \nabla(\delta \boldsymbol{u}) \mathrm{d}V = \int_\Omega \boldsymbol{b} \cdot \delta \boldsymbol{u} \mathrm{d}V + \int_{\partial\Omega} \boldsymbol{t} \cdot \delta \boldsymbol{u} \mathrm{d}S \tag{28}$$

And that for the phase-field evolution is written as [56]:

$$\int_\Omega \big[(2\mathcal{H} + \frac{g_c}{l_d})d + \eta_d \dot{d}\big] \delta d \mathrm{d}V + \int_\Omega g_c l_d \nabla d \cdot \nabla(\delta d) \mathrm{d}V = \int_\Omega 2\mathcal{H} \delta d \mathrm{d}V \tag{29}$$

3.2. Time discretization

The total loading history (designed by the time T) is divided into a number of incremental steps such as $t = 0, t_1, t_2, ..., t_n, t_{n+1}, ..., T$. For the current loading step $n+1$, the time increment is denoted as $\Delta t = t_{n+1} - t_n$. For the sake of simplicity, the evolution rate of d is assumed to be constant in the time increment under consideration, and it is calculated by:

$$\dot{d} = \frac{d_{n+1} - d_n}{\Delta t} \tag{30}$$

where d_n and d_{n+1} represent the damage values at the loading steps t_n and t_{n+1}, respectively.

Further, starting from the initial state, the value at the end of previous step t_n is known, the current viscoplastic strain is calculated by:

$$\boldsymbol{\varepsilon}^{vp}_{n+1} = \boldsymbol{\varepsilon}^{vp}_{n} + \int_{t_n}^{t_{n+1}} \dot{\boldsymbol{\varepsilon}}^{vp}(\tau)\mathrm{d}\tau \tag{31}$$

where $\boldsymbol{\varepsilon}^{vp}_{n}$ and $\boldsymbol{\varepsilon}^{vp}_{n+1}$ are the accumulated viscoplastic strains at the time steps t_n and t_{n+1} respectively. Again for the simplicity, the viscoplastic strain rate is considered to be constant and determined by the state at the loading step t_n with Equation (11). Thus, the accumulated viscoplastic strain for the current step is given by:

$$\boldsymbol{\varepsilon}^{vp}_{n+1} = \boldsymbol{\varepsilon}^{vp}_{n} + \Delta t \dot{\varepsilon}^{vp}(t_n) \tag{32}$$

It iw worth noticing that due to the simplified explicit time integration scheme adopted here, a small time increment should be chosen for a stable numerical solution. In general, preliminary calculations are performed in order to choose a suitable time increment.

With the time discretization scheme presented above, the weak form integrals for the current loading step t_{n+1} are rewritten as:

$$\int_\Omega \left\{\mathbb{C}(d_{n+1}) : \left[\boldsymbol{\varepsilon}_{n+1} - \boldsymbol{\varepsilon}^{vp}_{n+1}\right]\right\} : \nabla(\delta \boldsymbol{u})\mathrm{d}V = \int_\Omega \boldsymbol{b}\cdot\delta\boldsymbol{u}\mathrm{d}V + \int_{\partial\Omega} \boldsymbol{t}\cdot\delta\boldsymbol{u}\mathrm{d}S \tag{33}$$

and

$$\int_\Omega \left[(2\mathcal{H}_{n+1} + \frac{g_c}{l_d})d_{n+1} + \eta_d \frac{d_{n+1} - d_n}{\Delta t}\right]\delta d\mathrm{d}V + \int_\Omega g_c l_d \nabla d_{n+1}\cdot\nabla(\delta d)\mathrm{d}V = \int_\Omega 2\mathcal{H}_{n+1}\delta d\mathrm{d}V \tag{34}$$

It is noticed that H_{n+1} is calculated from the values of $\boldsymbol{\varepsilon}_{n+1}$ and $\boldsymbol{\varepsilon}^{vp}_{n+1}$.

3.3. Geometrical discretization

The computational structure domain Ω is divided into n_e elements which are defined by n_p nodes. The target here is to determine, at each loading step, the nodal values of displacement components denoted by the vector $\boldsymbol{U}$ and those of phase-field variable by $\boldsymbol{d}$. Classically, the displacement and damage fields are approximated in terms of their nodal values by using suitable shape functions. Their gradient functions are accordingly calculated:

$$\begin{aligned} \boldsymbol{u}(\boldsymbol{x}) &= \boldsymbol{N}_u(\boldsymbol{x})\boldsymbol{U}^e \qquad & d(\boldsymbol{x}) &= \boldsymbol{N}_d(\boldsymbol{x})\boldsymbol{d}^e \\ \boldsymbol{\varepsilon}(\boldsymbol{x}) &= \boldsymbol{B}_u(\boldsymbol{x})\boldsymbol{U}^e \qquad & \nabla d(\boldsymbol{x}) &= \boldsymbol{B}_d(\boldsymbol{x})\boldsymbol{d}^e \end{aligned} \tag{35}$$

where $\boldsymbol{N}_u(\boldsymbol{x})$, $\boldsymbol{B}_u(\boldsymbol{x})$ and $\boldsymbol{N}_d(\boldsymbol{x})$, $\boldsymbol{B}_d(\boldsymbol{x})$ are the matrices of shape functions and their derivatives for the displacement and damage fields, respectively. For the sake of simplicity, the same shape functions are usually used for both fields and their test ones. More details can be found in [67, 56, 71]. With the geometrical discretization and elementary approximation presented above, the weak form integrals (33) and (34) are transformed into two systems of discrete equations:

$$\begin{cases} \boldsymbol{K}_u \boldsymbol{U}_{n+1} = \boldsymbol{F}^{ext}_{u,n+1} + \boldsymbol{F}^{vp}_{n+1} \\ \boldsymbol{K}_d \boldsymbol{d}_{n+1} = \boldsymbol{F}_{d,n+1} \end{cases} \tag{36}$$

$\boldsymbol{K}_u$ and $\boldsymbol{K}_d$ are the global stiffness matrices, $\boldsymbol{F}^{ext}_{u,n+1}$, $\boldsymbol{F}_{d,n+1}$ the global nodal forces vectors, respectively for the displacement and damage fields, and $\boldsymbol{F}^{vp}_{n+1}$ the global nodal force vector related to viscoplastic flow:

$$\begin{cases} \boldsymbol{K}_u = \displaystyle\int_\Omega \Big[\boldsymbol{B}_u^T \mathbb{C}(d_{n+1}) \boldsymbol{B}_u\Big] \mathrm{d}V \\ \boldsymbol{F}^{ext}_{u,n+1} = \displaystyle\int_\Omega \big[\boldsymbol{N}_u^T \cdot \boldsymbol{b}\big] \mathrm{d}V + \int_{\partial\Omega} \big[\boldsymbol{N}_u^T \cdot \boldsymbol{t}\big] \mathrm{d}S \\ \boldsymbol{F}^{vp}_{n+1} = \displaystyle\int_\Omega \Big[\boldsymbol{B}_u^T \mathbb{C}(d_{n+1}) : \boldsymbol{\varepsilon}^{vp}_{n+1}\Big] \mathrm{d}V \end{cases} \tag{37}$$

and

$$\begin{cases} \boldsymbol{K}_d = \displaystyle\int_\Omega \Big[(\frac{g_c}{l_d} + 2\mathcal{H}_{n+1} + \frac{\eta_d}{\Delta t}) \boldsymbol{N}_d^T \boldsymbol{N}_d + g_c l_d \boldsymbol{B}_d^T \boldsymbol{B}_d\Big] \mathrm{d}V \\ \boldsymbol{F}_{d,n+1} = \displaystyle\int_\Omega (2\mathcal{H}_{n+1} + \frac{\eta_d}{\Delta t} d_n) \boldsymbol{N}_d^T \mathrm{d}V \end{cases} \tag{38}$$

3.4. Staged coupling algorithm

It is worth noticing that the displacement (and stress) and cracking evolution problems are strongly coupled. Indeed, the displacement (stress) evolution is affected by the damage process. For instance, the elastic stiffness tensor and viscoplastic threshold are functions of damage variable. Inversely, the damage evolution is driven by the mechanical field through the stored elastic and viscoplastic energy. Therefore, both problems should be solved in a coupled way. However, it is demonstrated that the energy history functional $\mathcal{H}(t)$ given in (38) is non-convex with respect to the couple of unknowns ($\boldsymbol{u}$, d) [44, 66]. As a consequence, it is difficult to solve the systems of coupled equations (36) by using the conventional Newton-Raphson procedure. However, the functional $\mathcal{H}(t)$ is convex with respect to one of two unknowns ($\boldsymbol{u}$ or d), if the other one is fixed. In general, the so-called alternating minimization (AM) solver proposed in [44, 66] is widely used and adopted here. In the AM solver, two solution stages are successively performed at the k^{th} iteration of a specific loading step $n+1$. This is summarized as follows:

Stage-1: Solving the displacement problem with the damage field fixed at $\boldsymbol{d}_{n+1}^{k-1}$ obtained from the last iteration:

$$\boldsymbol{U}_{n+1}^{k} = [\boldsymbol{K}_{u}^{k-1}(\mathbb{C})]^{-1} \cdot \left[\boldsymbol{F}_{u,n+1}^{ext} + \boldsymbol{F}_{n+1}^{vp}\right] \text{ , with } \mathbb{C} = \mathbb{C}(\boldsymbol{d}_{n+1}^{k-1})$$

Stage-2: Solving the phase-field problem using the updated displacement field and history energy functional:

$$\boldsymbol{d}_{n+1}^{k} = [\boldsymbol{K}_{d}^{k}]^{-1} \cdot \boldsymbol{F}_{d,n+1}^{k}(\mathcal{H}) \text{ , with } \mathcal{H}_{n+1}^{k} = \mathcal{H}(\boldsymbol{U}_{n+1}^{k})$$

These two stages are repeated until the convergence criterion $\|\boldsymbol{d}_{n+1}^{k} - \boldsymbol{d}_{n+1}^{k-1}\| \leq \epsilon$ is verified. According to [38], a convergence tolerance is taken as $\epsilon = 1 \times 10^{-5}$.

4. Simulation of laboratory tests on Jinping marble

In view of assessing the efficiency of time-dependent phase-field model, representative laboratory tests are investigated in this section. It is worth noticing that the emphasis of phase-field model is to capture the progressive damage toward cracking process. For the sake of simplicity, instantaneous plastic deformation is not taken into account. Inelastic strains, failure and post-failure softening are entirely attributed to damage evolution and localization as well as viscoplastic flow. Therefore, the proposed phase-field model is mainly suitable for brittle rocks under low confining pressure. For this reason, a typical brittle rock, Jinping marble, is here selected. This rock has been widely investigated in the context of stability analysis of high slopes around the Jinping I hydraulic power plant.

Short term triaxial compression tests and long term creep tests are considered. Representative experimental data are selected from previous studies [12, 13]. The laboratory tests were performed on cylindrical samples of 50 mm in diameter and 100 mm in height. For the sake of simplicity, two-dimensional plane strain simulations are performed. The specimen geometrical domain is divided into 200×400 (80 000) elements. According to experimental observations [12, 13], failure patterns of samples are mainly characterized by localized fractures even if the samples are subjected to uniform macroscopic stresses and displacements. The onset of localized fractures or non-uniform stress and strain fields is generally related to material heterogeneity. Without detailed descriptions of such heterogeneity of tested samples and in order to enhance the onset of localized fractures, a small weak region (one element) is placed at the sample center where the value of g_c is reduced by 1%. The boundary conditions are composed of a uniform normal stress on the lateral surfaces (denoted as σ_3) and a uniform vertical displacement on the upper boundary surface, which is used to calculate the average axial strain ϵ_1. As output results, on obtains the average lateral strain ϵ_3 and axial stress σ_1.

4.1. Short term triaxial tests

For modeling of short term mechanical behavior, two elastic parameters and the critical energy release rate g_c should be identified. The elastic parameters of Jinping marble are

directly taken from the previous experimental studies [12] and the following values are used: Young's modulus $E = 45000\ MPa$ and Poisson's ratio $\nu = 0.15$. The critical fracture energy (or energy release rate) g_c is a key parameter in the phase-field model. Its value is generally identified form uniaxial tension or bending tests, which are not available for the studied rock. Further, it is found that the value of g_c identified from tensile test could not be suitable for cracking under compressive stresses [50, 51]. However, the value of g_c can be indirectly estimated from the peak values of deviatoric stress obtained in triaxial compression tests. Moreover, it is found that for most rocks, the values of g_c can vary with confining stress. Inspired by the previous studies [50, 51], the following empirical relation is here adopted: $g_c = g_{c0}e^{b(p_c/p_r)}$, with p_c being the confining stress and $p_r = 1MPa$ the reference normalizing pressure. g_{c0} denotes the value of g_c for uniaxial compression with $p_c = 0$ and the parameter b controls its variation with confining stress. For the case of Jinping marble studied here, by using the peak deviatoric stresses obtained in three triaxial compression tests respectively with 0, 10 and 20 MPa confining stress, we have obtained $g_{c0} = 2.0937N/mm$ and $b = 0.0466$. Finally, the length scale parameter l_d is generally taken as 1 to 3 times of the smallest element size. It is set here to 0.25 mm.

Comparisons between experimental data and simulation results are presented in Figure 1 for three values of confining pressure. The main features of mechanical behavior of Jinping marble are correctly reproduced by the relatively simple phase-field model. The values of peak deviatoric stress are well predicted. For low confining pressures (0 and 10 MPa), the post-peak brittle failure process is also properly described. For the test with a high confining pressure (20 MPa), it seems that the marble exhibits a brittle-ductile transition. Quite large plastic strains, in particular in the radial direction, are observed. There is a residual strength in the post-peak regime due to the frictional effect along closed cracks. All these features are not properly captured by the simple elastic-brittle model as it is not the emphasis of the present work. However, these features can be improved by incorporating an instantaneous plastic deformation mechanism in the phase-field model or/and taking into account the friction effect along localized cracks. This will be performed in our future studies.

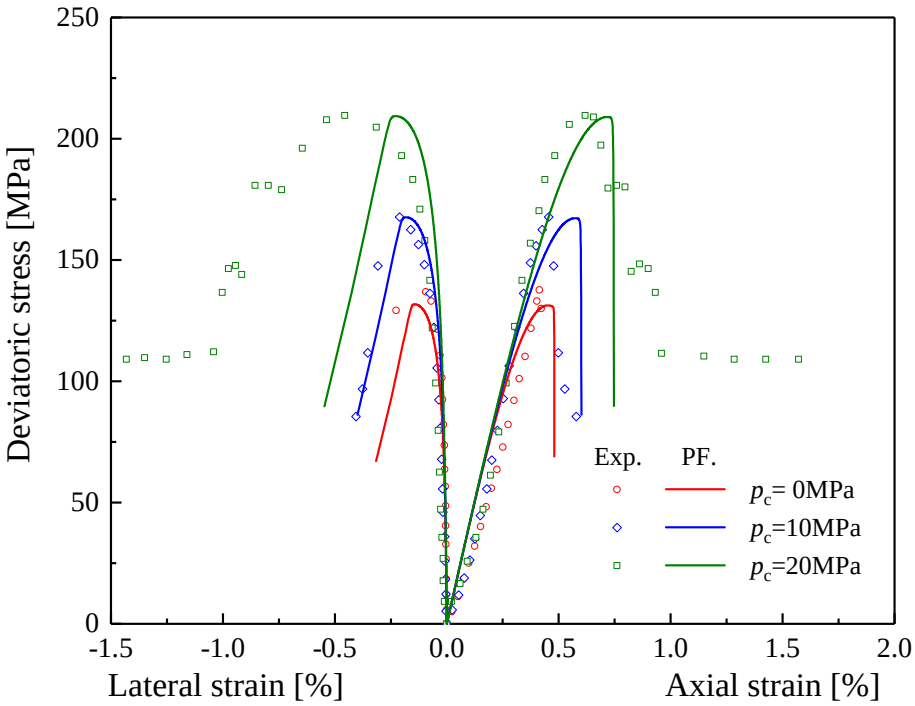

Figure 1: Axial and radial strains versus deviatoric stress of Jinping marble in triaxial compression tests with different pressures: comparisons between numerical results and experimental data [12]

4.2. Uniaxial and triaxial creep tests

At first, an uniaxial compression creep test reported in [12] is considered. Five additional parameters involved in the viscoplastic model should be identified, say η, σ_s, c_v, n and m. These parameters cannot be directly calculated from experimental measurements and they are generally calibrated from the optimal numerical fitting of creep tests. Basically, the parameter σ_s defines the threshold of viscoplastic flow and can be determined at the end of elastic stage in a triaxial creep test. η mainly controls the initial creep rate during the primary creep stage while n affects the creep rate evolution. m describe the viscoplastic hardening effect on the transition from the primary to secondly creep stages. The viscoplastic potential parameter c_v controls the volumetric viscoplastic strain and can be identified from the lateral creep strain curve. For the marble samples tested in [12], the following values of viscoplastic parameters are obtained: $\eta = 1 \times 10^{-7} s^{-1}$, $\sigma_s = 100$ MPa, $c_v = 0.01$, $n = 3.2$ and $m = 7980$. In Figure 2, we show the axial and radial strains as functions of time under

an axial stress of 113 MPa. The evolution of damage is also reported. It is found that the numerical predictions obtained using the elastic-viscoplastic and phase-field model are in good agreement with the experimental data. The main features of creep deformation behavior of Jinping marble are well described by the proposed model. In particular, typical three stages of creep deformation are found in this test, namely an increasing primary creep stage, an quasi-stationary stage and an accelerating one leading to the sample failure. It is further to observe the creep deformation rate is clearly linked to the damage evolution which also exhibits three distinct stages. During the first stage, the damage increases quickly due to the applied axial stress. Then it evolves slowly with the viscoplastic strain. Finally, the maximum value in the sample increases very rapidly and reaches 1 causing the macroscopic failure of sample.

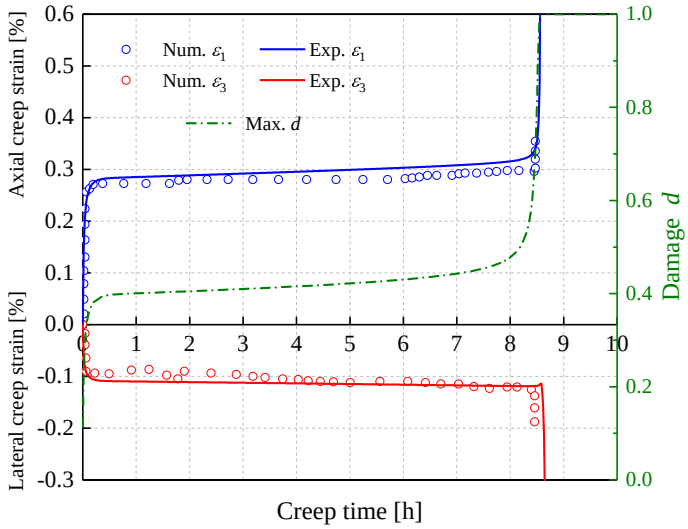

Figure 2: Evolution of axial and lateral strains as well as damage variable with time in an uniaxial compression creep test under an axial stress of 113 MPa: comparisons between numerical results and experimental data [12]

In Figure 3, we show the damage variable distributions inside the sample obtained at different instances during the uniaxial compression creep test. Due to the presence of weak element, the damage localization starts from the center of sample. Two quasi symmetric localized damage bands are obtained. This configuration is close to fracture modes widely

observed in rock samples [12]. It is worth noticing that the use of a weak element is an artificial technique to facilitate the onset of damage localization. In future studies, this point can be addressed by considering the spatial variability of micro-structure of rocks such as porosity and mineral composition.

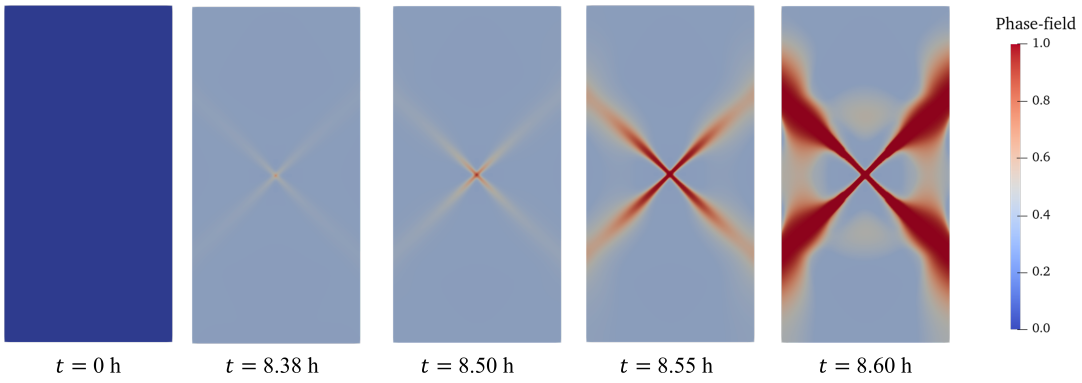

Figure 3: Evolution of damage distribution of uniaxial compression creep test

Moreover, two triaxial compression creep tests under a confining pressure of 30MPa, also performed on Jinping marble respectively with a single and multiple deviatoric stress steps, are investigated. The experimental data are taken from [13]. The samples used in these tests and those used in [12] were drilled at different zones. Therefore, there are some quantitative differences on mechanical parameters. For instance, the elastic properties measured in triaxial compression tests [13] are as follow: Young's modulus $E = 30000\ MPa$ and Poisson's ratio $\nu = 0.15$. The critical fracture energy g_c is again fitted from the peak deviatoric stress and one gets $g_c = 1.2775\ N/mm$. The parameters for viscoplastic flow are as follows: $\eta_d = 1 \times 10^{-10} Ns/mm^2$, $\eta = 1 \times 10^{-7} s^{-1}$, $\sigma_s = 70MPa$, $c_v = 0.26$, $n = 2.4$ and $m = 1080$. However, the same finite element mesh and the same value of length scale l_d as those in the uniaxial creep test are used.

Table 1: Reference set of model's parameters for rock samples investigated in [13]

Elastic and phase-field parameters	E (MPa)	ν (-)	g_c (N/mm)	p_c (MPa)	l_d (mm)
Values	30000	0.15	1.2775	30	0.25
Viscoplastic parameters	η (s^{-1})	σ_s (MPa)	n (-)	m (-)	c_v (-)
Values	1×10^{-7}	70	2.4	1080	0.26

The creep test with a single loading step was performed under a deviatoric stress of 143 MPa. Numerical predictions are compared with experimental data in Figure 4(a), together with the damage variable evolution. A good concordance is obtained. In this test, one obtains mainly a primary creep phase. Both axial and radial strains evolve towards stationary values and creep strain rates decrease with time. Another important feature is that the radial creep strain is clearly larger than the axial one. This means that the viscoplastic deformation induces an important volumetric dilatance. In the second test, four loading steps were realized with increasing values of deviatoric stress from 65 MPa to 130 MPa. Comparisons between numerical results and experimental data of axial and radial strains are shown in Figure 4(b). It is interesting to observe that the creep strain rate increases with the rise of deviatoric stress. When this one is high, a small increment of deviatoric stress can generate large creep strains, for instance during the last loading step with an increment of 10 MPa. The damage variable evolution trend is fully consistent with that of strains. Again, the radial creep strain is clearly larger than the axial one. There is a good agreement between numerical and experimental results for the axial strain as well as for the radial one when the deviatoric stress is low (the first two loading steps). But more and more scatters are observed when the deviatoric stress is high (the last two steps). This indicates that the volumetric dilation is enhanced during creep process by material damage.

As a possible improvement of the viscoplastic model, the volumetric dilation parameter c_v should evolve with damage.

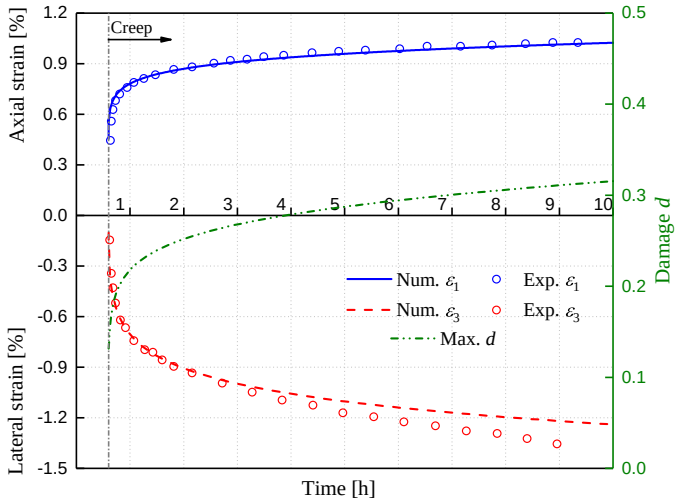

(a) creep test with a single loading step ($q = 143MPa$)

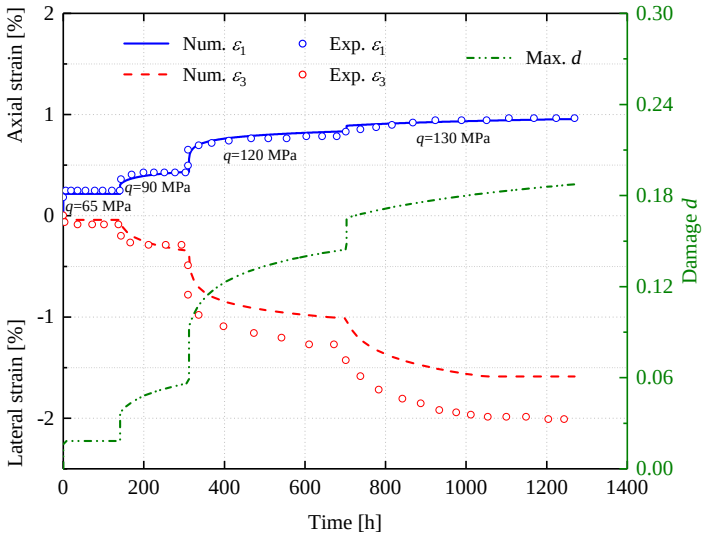

(b) creep test with multiple loading steps

Figure 4: Variations of axial and lateral strains in triaxial compression creep tests under a confining pressure of 30 MPa respectively with a single and multiple loading steps, together with damage variable evolution

4.3. Sensitive analysis

Some comparative calculations are presented here in order to investigate effects of some key parameters on short and long-term mechanical responses of rocks.

Firstly, the influences of geometry discretization as well as the characteristic length are studied. For this purpose, six cases with different minimum element size h and length scale l_d are considered and detailed in Table 2. These case are chosen for the following strategy. In the cases 1 to 4, the characteristic length is equal to or higher than the minimum element size, $l_d \geq h$, while in the cases 5 and 6, it is smaller than the minimum element size $l_d < h$. Moreover, in order to facilitate the comparison and interpretation, the value of g_c is accordingly reset with that of the length scale l_d. The objective is to obtain a very close value of uniaxial compression strength for all the cases considered to that reported in [12].

Table 2: Different sets of considered parameters for sensitivity study of uniaxial compression test reported in [12]

Case No.	l_d (mm)	h (mm)	g_c (N/mm)	Case No.	l_d (mm)	h (mm)	g_c (N/mm)
1	1.0	1.0	2.08	4	1.0	0.5	2.08
2	0.5	0.5	1.04	5	0.5	1.0	1.04
3	0.25	0.25	0.52	6	0.25	0.5	0.52

In Figure 5, we first show the overall strain-stress curves of uniaxial compression test for six cases considered in Table 2. It is confirmed that all six cases give a quasi identical uniaxial compression strength. However, the responses are slightly different in the post-peak regime. For those cases where $l_d \geq h$ (cases 1-4), the mechanical behavior is almost the same while the curves of the cases where $l_d < h$ (cases 5, 6) are lower than the other cases. However, significant differences are observed in the uniaxial creep test as shown in the same figure. Although the similar primary creep stages are obtained, the period of quasi constant creep rate for the cases with $l_d < h$ (cases 5, 6) is clearly shorter than those with $l_d \geq h$ (cases 1-4). In other words, the accelerated creep stage occurs earlier. According

these results, it is recommended to ensure the condition of $l_d \geq h$ in order to obtain the stable numerical results in both pre- and post-peak regimes.

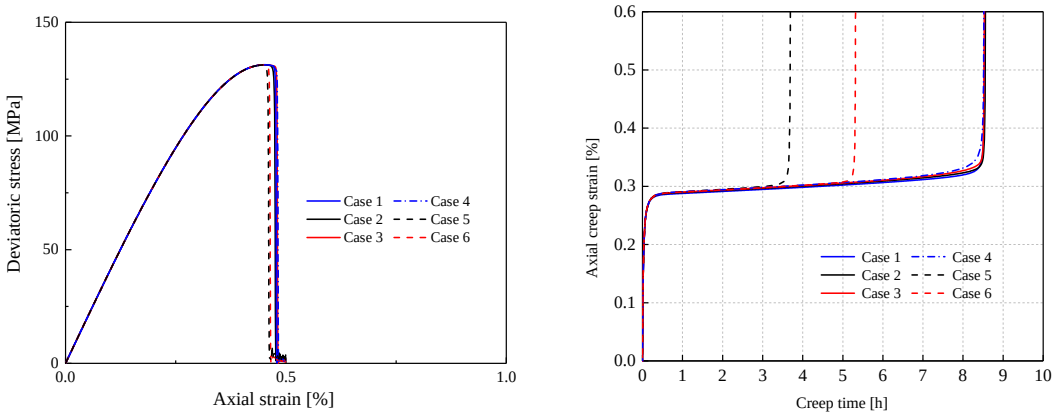

Figure 5: Influence of characteristic length and mesh size on overall strain-stress curve in uniaxial compression test (left) and on strain evolution in uniaxial compression creep test (right)

On the other hand, the influence of length scale parameter l_d and mesh size on cracking pattern is also investigated and presented in Figure 6. One can clearly see that it is the length parameter l_d that controls the width of localized cracks (damaged zones) rather than the mesh size h. For instance, both the cases 1 and 4 show a very similar distribution of damage variable though they have different element size. At the same time, with the decrease of l_d, the width of localized cracked zones becomes finer from the case 1 to 3.

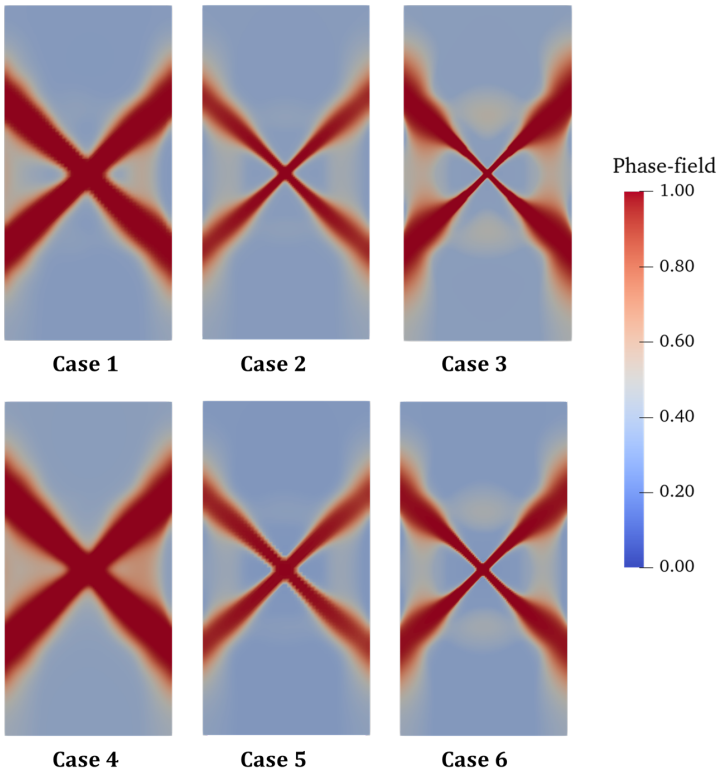

Figure 6: Distribution of damage in uniaxial compression creep test in different cases

The coupling effect of viscoplastic flow and damage evolution is considered. Indeed, in the proposed viscoplastic model, the viscoplastic threshold is weakened by the damage growth though the degradation function $g_{vp}(d)$ introduced in the loading function f^{vp} (12). Two calculations are performed on the uniaxial creep test by respectively considering that the viscoplastic threshold is affected $g_{vp}(d) = (1-d)^2$ or not affected $g_{vp}(d) = 1$ by the damage evolution. Comparisons between two cases are presented in Figure 7. One can see that in the case without degradation, an primary creep is obtained. However, due to the degradation of viscoplastic threshold by damage, three creep stages are observed. The creep strains during the primary stage are much larger than those in the case without degradation. After a period of quasi constant creep rate, an accelerated creep stage occurs and leads to a rapid failure. These results show that the damage degradation effect can play an essential role in time-dependent deformation of rocks.

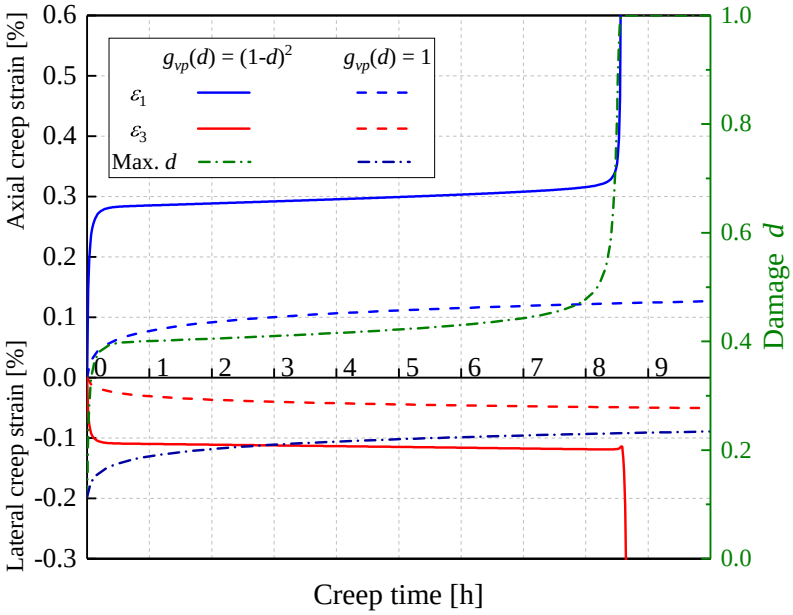

Figure 7: Influence of damage degradation effect on viscoplastic flow in uniaxial creep test

In the second example, the influence of critical fracture energy g_c on creep deformation is studied. For this purpose, three different values of g_c ($1.225N/mm$, $1.2375N/mm$, $1.2775N/mm$) are used in simulations of the triaxial creep test with one-step axial loading. Comparisons between three calculations are presented in Figure 8 in terms of variations of strains and damage variable. It is obvious that the damage evolution rate is higher when the value of g_c is lower. Accordingly, the rate of creep strains is also enhanced by the decrease of critical fracture energy. In the case with $g_c = 1.225N/mm$, it seems that the damage variable evolves towards a stationary value. In the case with $g_c = 1.2375N/mm$, the damage evolution rate evolves to a constant value. Finally, In the case of $g_c = 1.2775N/mm$, the damage evolution rate is accelerated after a period of time and evolves towards to unit, producing an accelerated creep phase. There is a close connection between time-dependent deformation and damage evolution.

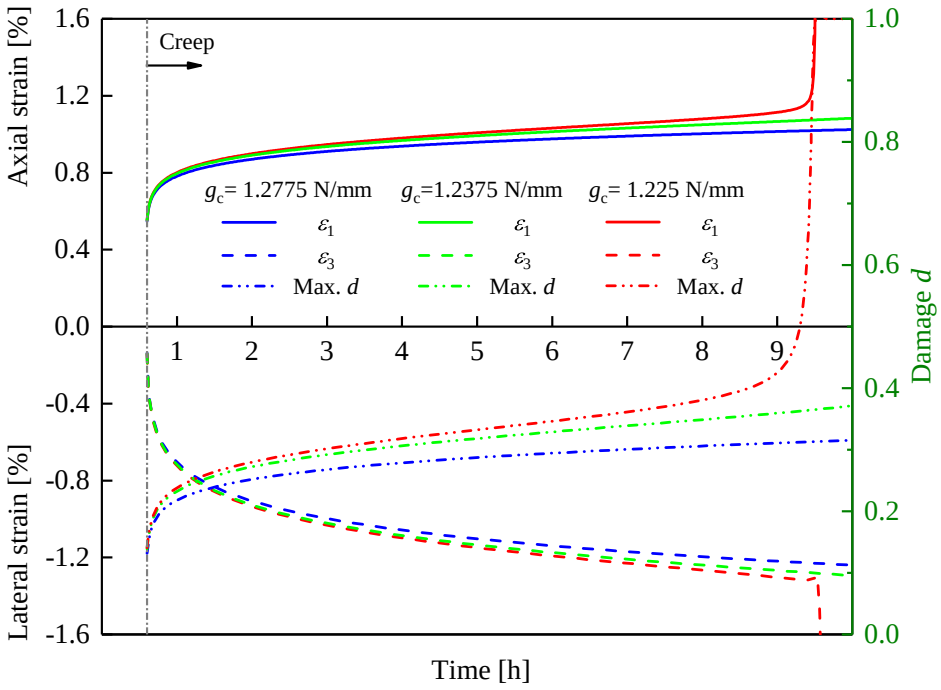

Figure 8: Influences of critical fracture energy g_c on time-dependent strains and damage evolution in a triaxial compression creep test with a confining pressure of 30 MPa

Moreover, as a time-dependent viscoplastic phase-field model is used in this study, the time-discretization scheme can affect the obtained numerical results. For this purpose, the sensitivity of creep deformation to the time increment size is here investigated. Four different values of Δt are chosen and compared. The obtained results are presented in Figure 9(a). It can be seen that the creep strain curves become almost unchanged when the time increment is less than $1.0s$. As a consequent, the this value of $\Delta t = 1.0s$ is chosen in all calculations of this section. In addition, the influences of two viscoplastic parameters η and n on creep strain are also studied. It is shown that η mainly controls the initial creep rate during the primary stage. As presented in Figure 9(b), higher the value of parameter η is, bigger the slope of primary creep curve is. The parameter n affects the creep rate evolution. On other word, the creep rate reduces quickly when a small value of n is used, as shown in Figure 9(c).

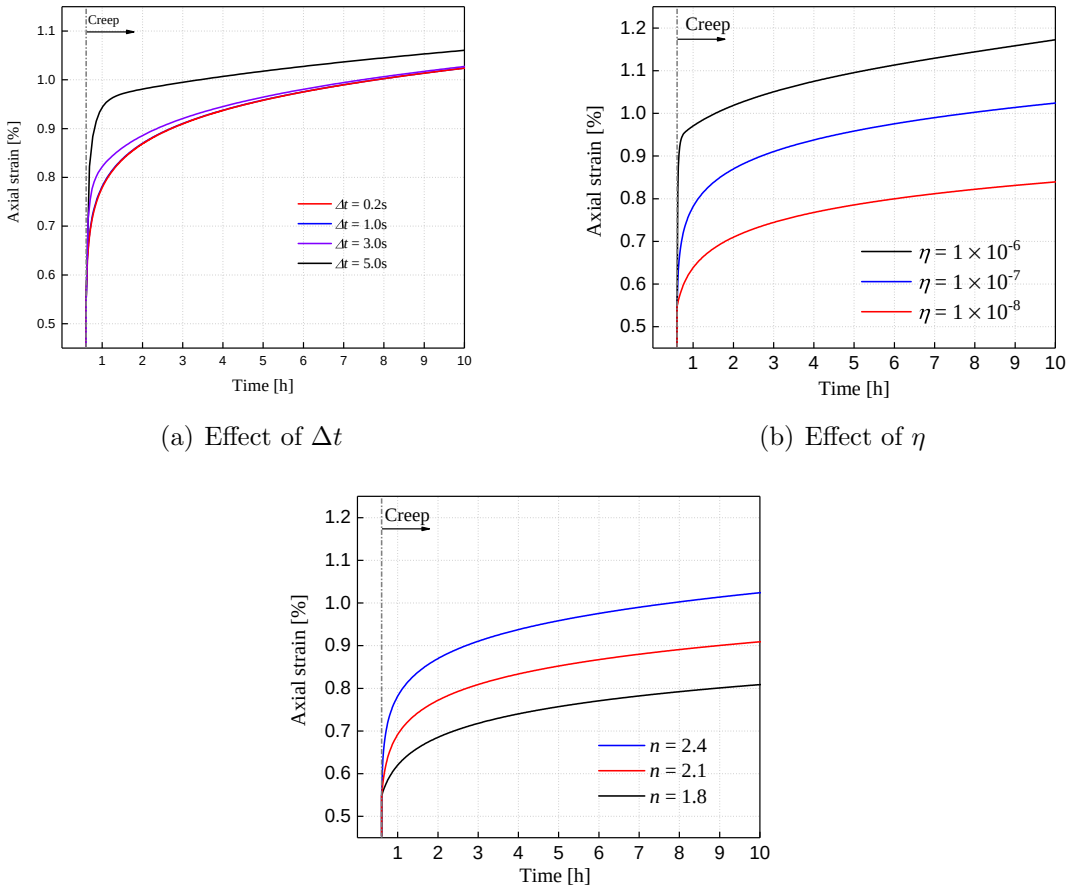

(a) Effect of Δt

(b) Effect of η

(c) Effect of n

Figure 9: Sensitive analysis of time increment and two viscoplastic parameters in a triaxial compression creep test with a confining pressure of 30 MPa

5. Time-dependent behavior of left bank high slope of Jinping I hydropower station

As an example of engineering application, time-dependent mechanical responses of the left bank high slope of Jinping I hydropower plant are not investigated by using the proposed phase-field model.

5.1. Summary of engineering geological conditions

The Jinping I hydropower station, one of the highest and largest ones all over the world, is built at the Pusiluogou in the west of Great River Bend of Yalong River which is adjacent to Muli and Yanyuan counties in Liangshan Yi Autonomous Region. It is near Xichang

(27°32′-28°10′N, 101°46′-102°25′E), about 500 km southwest of Chengdu, Sichuan Province, PR China. The double-curvature arch dam, of 305 m in height with a crest at 1885 m above the sea level (asl), is constructed in a typical V-shaped valley [72]. Due to the height of the dam, the retained reservoir level will reach 1880 m asl, with a total reservoir capacity 7.76 billion m^3 and the regulated storage 4.91 billion m^3.

The valley is cut through the Triassic Zagunao Formation which consists of sandstone, slate and marble. In view of its location between the Tibetan Plateau and Sichuan Basin, the area is characterized by complex geological conditions [73], especially on the left bank of the valley. A typical geological profile (L9-L9) of the left bank was reported in [17]. Accordingly the slope rises at an angle between 70°-80° below 1900 m asl and 40°-50° above. In addition, the bedrock of slope is composed of metamorphic rocks belonging to the Zagunao group of the middle and upper Triassic ($T_{2\text{-}3Z}$) which can be divided into three members [74]: a green schist member ($T^1_{2\text{-}3Z}$), a marble member ($T^2_{2\text{-}3Z}$) and a slate and low-grade metamorphic sandstone member ($T^3_{2\text{-}3Z}$). Moreover, a large number of faults and fractures are observed in this area [74], for instance, the fault referred as f_2 is shown in Figure 10(a). To sum up, the geological conditions at the dam site are extremely complex and request an in-depth investigation of stability conditions of the left abutment slope. In this context, the present study shall provide a numerical analysis of time-dependent deformation and damage by using an efficient phase-field method.

5.2. Description of numerical model

Here we consider the typical two-dimensional section L9-L9 of the left bank high slope of Jinping I hydro-power station. In Figure 10(a), the geometrical domain and main geological layers of the section are presented. The studied domain is of 370 m in width and of 450 m in height. The slope section composition is simplified to be composed of three principal rock layers respectively referred to as II, III and IV, and a major fault zone named as f_2. Based on the studies related to the laboratory tests presented above and field investigations [73, 17], the basic model's parameters of each layers are given in Table 3. As the fault zone f_2 is mainly constituted with filled materials, it is here considered as a thin layer with a

small critical fracture energy g_c. In Figure 10(b), one also shows the finite element mesh adopted in this study. It is composed of 12523 elements and 12729 nodes in total. The length scale parameter for the regularized crack description is taken as $l_d = 0.25\ m$, which is equal to the minimum size of element.

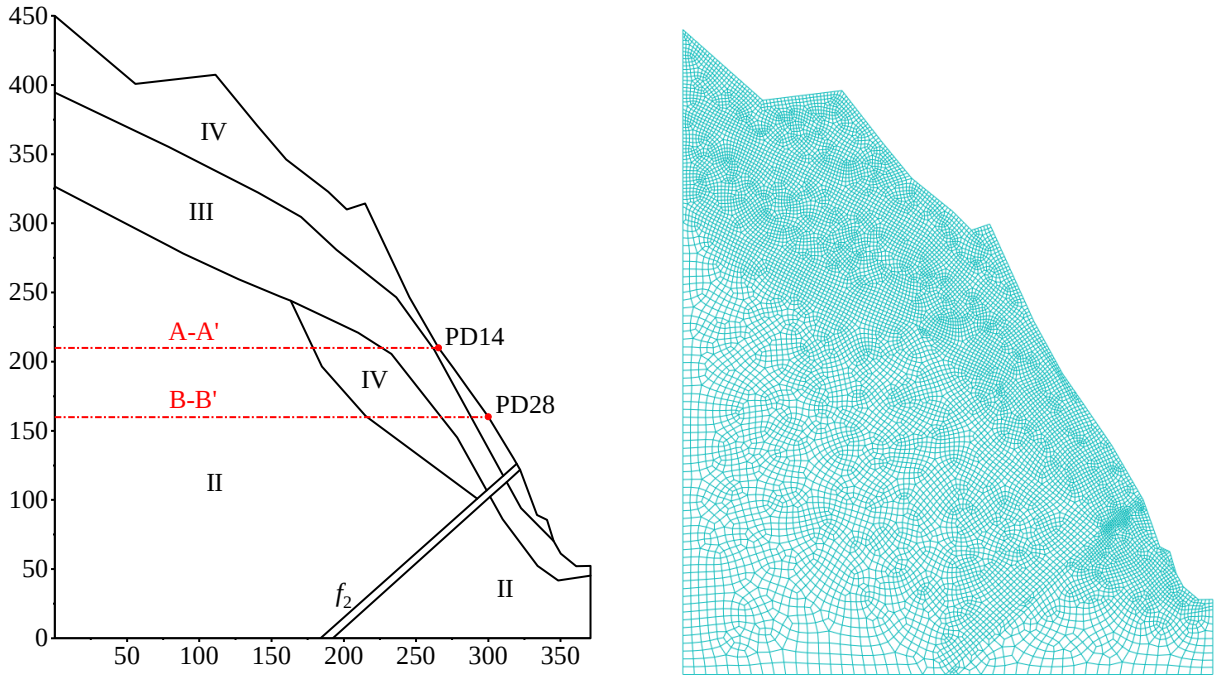

(a) composition of L9-L9 slope section

(b) finite element mesh generation

Figure 10: Geometrical domain of a selected slope section and finite element mesh generation

Table 3: Reference set of physical, elastic and phase-field parameters of different rock layers

	Rock layers			
	Layer II	Layer III	Layer IV	Fault f_2
Density ρ (kg/m^3)	2800	2700	2700	2600
Young's modulus E (MPa)	25000	8500	2500	3000
Poisson's ratio ν	0.23	0.26	0.3	0.28
Critical energy g_c (N/mm)	900	104	28.3	1.08

Table 4: Reference set of viscoplastic parameters

Parameters	η (s^{-1})	σ_s (MPa)	n (-)	m (-)	c_v (-)
Values	1×10^{-9}	5.8	2.8	1030	0.24

5.3. Main results of reference case

Main results obtained from a reference calculation using the parameters given in Tables 3 and 4 are first presented and discussed.

First of all, in Figure 11, the distributions of instantaneous displacement and damage induced by self gravity of slope are given. One can see that the maximum instantaneous displacement is obtained in the top zone of the slope. The fault layer is highly damaged. A small but not negligible damage distribution is also found inside the weak zone IV as shown in the Figure 11(b).

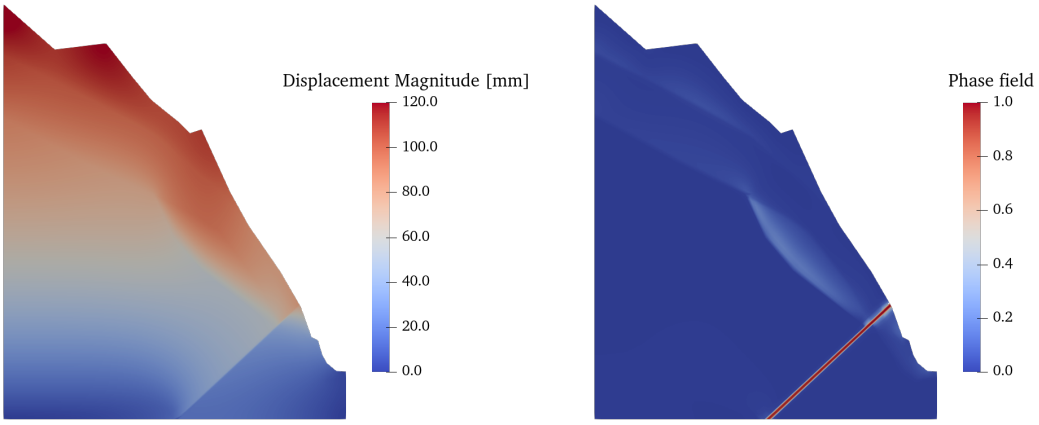

(a) Instantaneous displacement (b) Gravity induced damage

Figure 11: Instantaneous displacement and damage distributions induced by gravity effect inside the slope

The time-dependent behavior of the slope is then studied by taking the instantaneous results presented in Figure 11 as the initial conditions. As the gravity effect is already taken into account and there is no other applied loads, the long-term stability of the slope is entirely controlled by the time-dependent mechanical behavior of rock layers. Based on

the $in - situ$ measured data reported in [17], the time-dependent deformation of the slope during a forty month period (from 1^{st} January 2010 to 15^{th} April 2013)) is investigated in this work. Indeed, for the purpose of monitoring the deformation evolution of the left bank slope with the time, some monitoring points have been set, for instance the points $PD14$ and $PD28$ in the section $L9 - L9$ as shown in Figure 10(a). The comparison between the measured displacement and numerical prediction is presented in Figure 12. It seems that the numerical predicted evolution of displacement at the two monitoring points is in good agreement with the measured data.

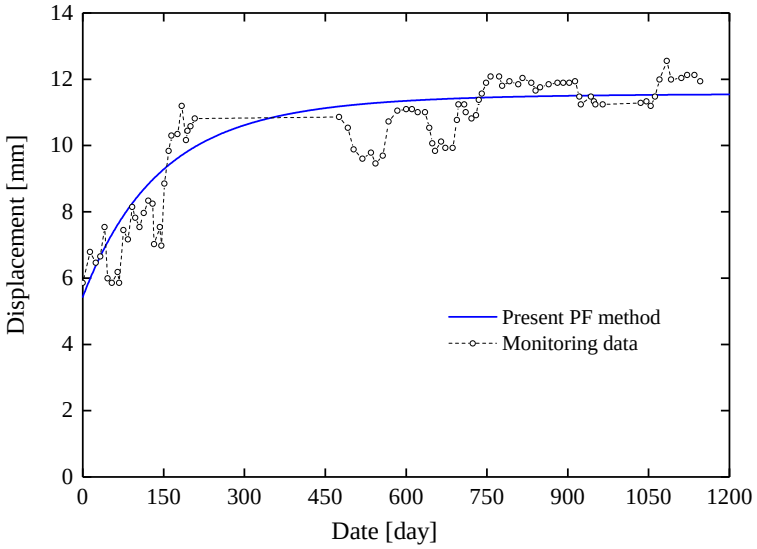

(a) monitoring point PD14

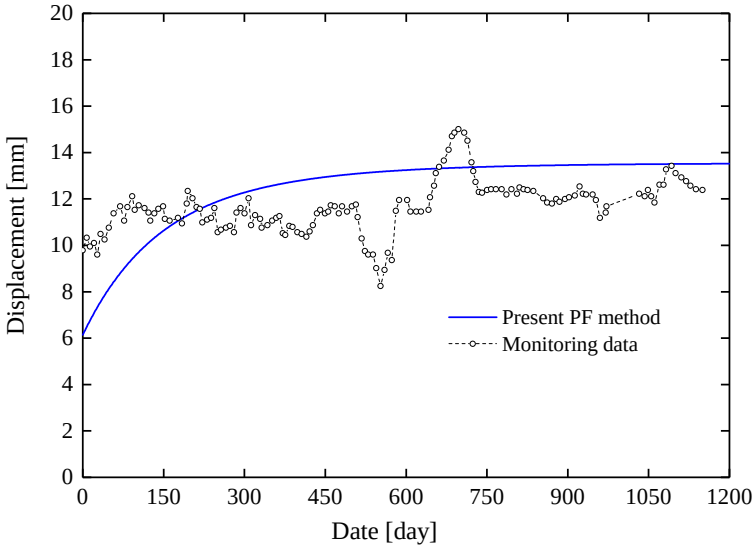

(b) monitoring point PD28

Figure 12: Comparisons of displacement evolution between measured and calculated values at two monitoring points (From 1^{st} January 2010 to 15^{th} April 2013)

The distribution of displacement and damage increments with respect to the instantaneous values at the end of calculation period (1200 days) are shown in Figure 13. Differently with the instantaneous results shown in Figure 11, the maximum time-dependent displacement increase is obtained inside the weak layer IV and around the fault layer f_2. At the same time, the damage distribution inside the weak layer IV exhibits a time-dependent growth. In order to show some quantitative examples, the variations of damage variable along two selected cut lines $A - A'$ and $B - B'$ defined in Figure 10(a) are also presented for three representative instances. One can see that the maximum damage value increases from 0.161 to 0.307 on the line $A - A'$ and 0.156 to 0.295 on $B - B'$. This clearly shows that the time-dependent damage evolution related to micro-crack growth is the main mechanism driving the time-dependent deformation of the slope.

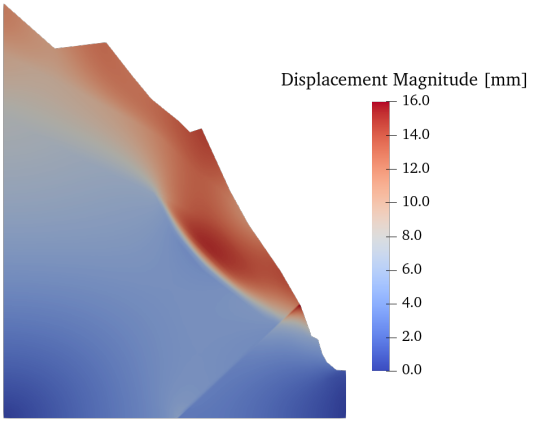

(a) Displacement increment

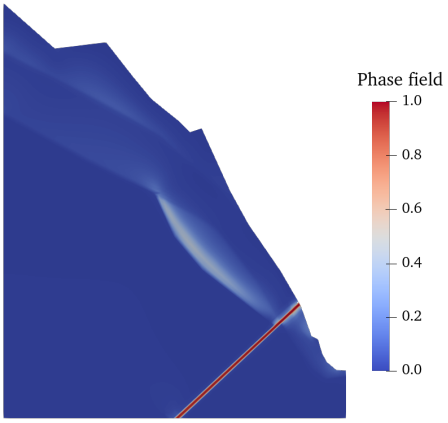

(b) Damage increment

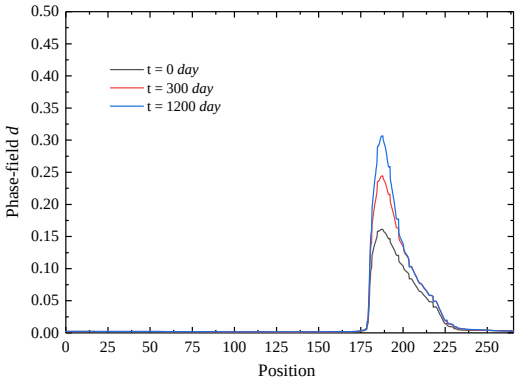

(c) Section $A - A'$

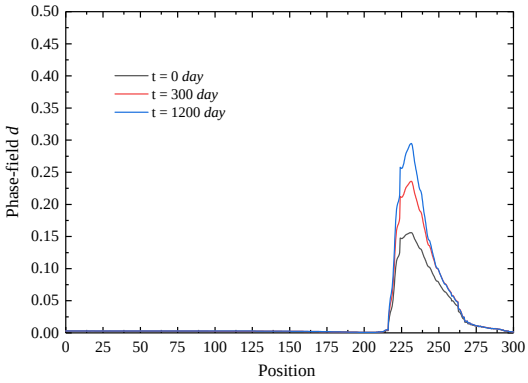

(d) Section $B - B'$

Figure 13: Distributions of displacement and damage increments with respect to the instantaneous values at the end of calculation period (1200 days), and variation of damage along the two cut lines defined in Figure 10(a) at three different instances

5.4. Sensitivity analysis of water weakening effect

Most slopes are subjected to water saturation change due to raining and reservoir level variation. It is also known that the mechanical properties of most rocks are sensitive to water content. In particular, a number of previous studies have shown that the critical fracture energy or stress intensity factor of rocks could be significantly reduced by an increase of water saturation degree [5, 75, 76]. In the case of the Jinping left bank slope, according to the experimental study reported in [77], the failure strength of all rock layers considered here can be reduced by 10% due to water saturation. Therefore, it is crucial to investigate the consequence of such water weakening effect of the long-term deformation and stability

of slopes.

However, as a first approximation, a simplified approach is adopted in this work. We shall not perform fully coupled hydromechanical calculations. The water weakening effect is taken into account simply by considering that the critical fracture energy g_c for each rock layer is reduced by different ratios. The predicted displacement evolution with time at the two monitoring points are presented in Figures 14 and 15 for two ratios of reduction. It is clear that the displacement is enhanced by the reduction of g_c. The amplification of displacement is quite small for a reduction of 5%. However, with a reduction of g_c by 10%, the displacements at two monitoring points are significantly amplified and exhibit an accelerating phase leading to sliding of slope. This seems to indicate that if the critical fracture energy parameter g_c is reduced by water saturation to some critical value, it is possible to generate the instability of slope.

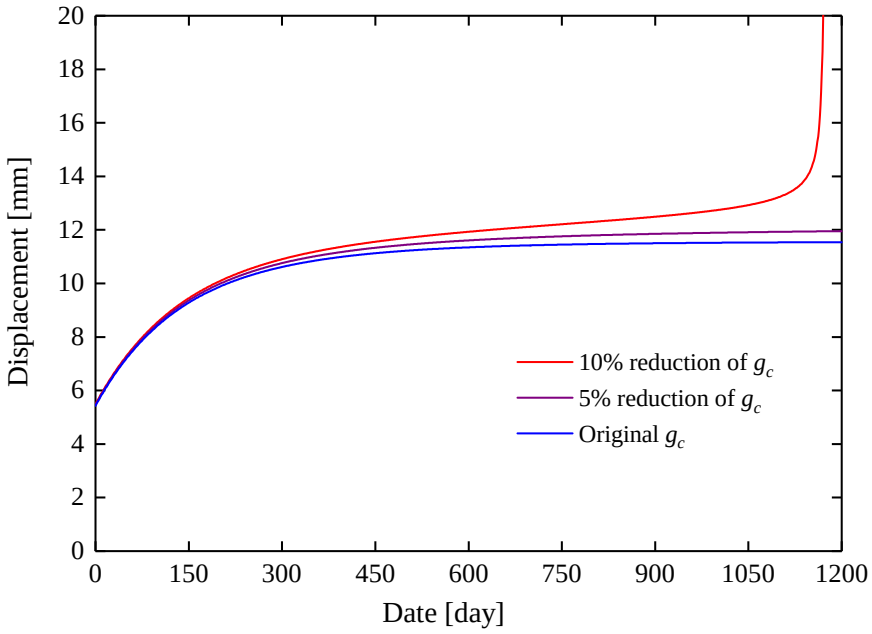

(a) Point PD14

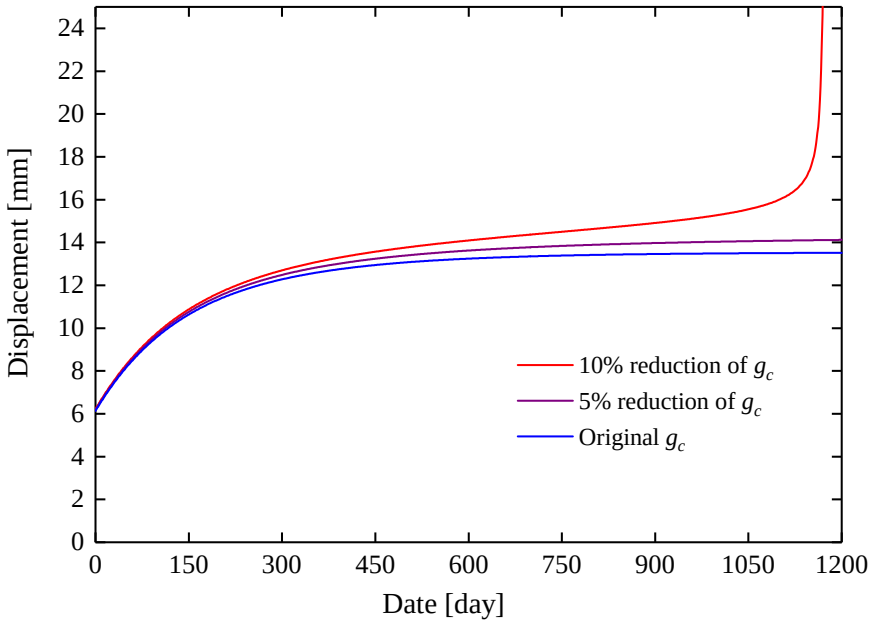

(b) Point PD28

Figure 14: Consequences of critical energy parameter g_c reduction on displacement evolution at two monitoring points

In order to better investigate the instability mechanism induced by the weakening of rock fracture resistance, in Figure 15, we show the damage variable distribution at six different time stages. One can see that at the first stage, the damage is mainly concentrated in the fault layer f_2 and the other zones are weakly affected by cracking process, as shown in Figure 15(a). Then, the damage zone propagates into the layer IV due to the increase of creep strains (see Figure 15(b)). There is further the coalescence of damage between these two layers causing macroscopic cracking (d close to 1) around the toe zone of the slope, as illustrated in Figure 15(c). From the stage d, the damaged zones propagate towards to the top region of the slope (see Figure 15(d) and 15(e)). Finally, in Figure 15(f), a large cracked band is formed and it leads to the instability of the slope.

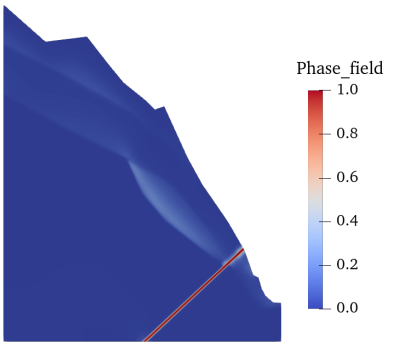

(a) $t = 0$ day

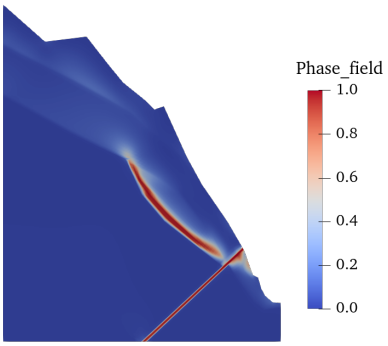

(b) $t = 1059$ day

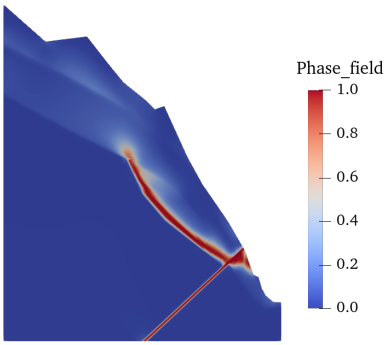

(c) $t = 1066$ day

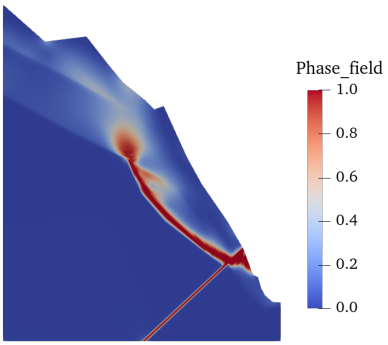

(d) $t = 1069$ day

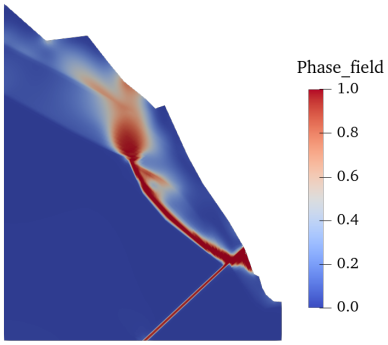

(e) $t = 1070$ day

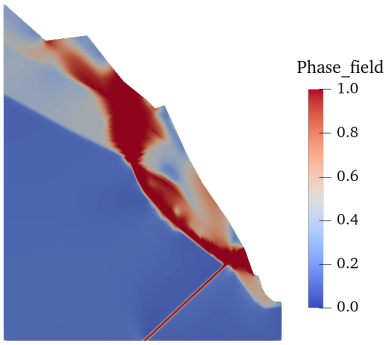

(f) $t = 1071$ day

Figure 15: Evolution of damage distribution at six different time stages

6. Conclusions

In this paper, we have proposed a new phase-field model for modeling the time-dependent cracking process of rocks. The viscoplastic deformation is coupled with the evolution of cracks. More precisely, the viscoplastic flow rate is enhanced by the induced damage through the weakening of creep threshold while the viscoplastic strain energy contributes to the damage evolution. The proposed model has been applied to describe the short and long term mechanical behavior of marble from the left bank of Jinping hydropower station. Numerical results were compared with experimental data from both laboratory tests and $in-situ$ measurements. It was found that the main features of marble mechanical responses were correctly described by the proposed model. The phase-field based model provides an efficient tool for modeling the transition from diffuse damage to localized cracks.

From the results obtained from the present study, it can be concluded that the induced damage is one of the keys mechanisms of brittle rocks such as marble. The macroscopic failure of those rocks is mainly due to the coalescence of micro-cracks leading to macroscopic fractures. The time-dependent evolution of damage or growth of micro-cracks is a key parameter controlling the long-term stability of structures in such rocks. Moreover, there is a strong interaction between viscoplastic deformation and damage evolution. It is crucial to take into account this type of interaction in long-term stability analysis of slopes. Furthermore, the weakening effect of water saturation on the fracture toughness of rocks is another key factor to be taken into account. Only a very simple approach has been adopted in this study. Further investigations should be performed for the in-depth characterization of the water weakening effect on long-term mechanical properties of those rocks in order to develop coupled hydromechanical modeling.

Acknowledgment

This study was partially supported by the National Key RD Program of China (Grant 2017YFC1501100).

References

1. Evans B, Fredrich JT, Wong TF. The brittle-ductile transition in rocks: Recent experimental and theoretical progress. *The Brittle-Ductile Transition in Rocks, Geophys Monogr Ser* 1990;56:1–20.
2. Wong Tf, Baud P. The brittle-ductile transition in porous rock: A review. *J Struct Geol* 2012;44:25–53.
3. Atkinson BK. Subcritical crack propagation in rocks: theory, experimental results and applications. *J Struct Geol* 1982;4:41–56.
4. Meredith PG, Atkinson BK. Fracture toughness and subcritical crack growth during high-temperature tensile deformation of westerly granite and black gabbro. *Phys Earth Planet Int* 1985;39:33–51.
5. Henry JP, Paquet J, Tancrez JP. Experimental study of crack propagation in calcite rocks. *Int J Rock Mech Min Sci Geomech Abstr* 1977;14:85–91.
6. Atkinson BK. Subcritical crack growth in geological materials. *J Geophys Res* 1984;89:4077–4114.
7. Nara Y, Kaneko K. Study of subcritical crack growth in andesite using the double torsion test. *Int J Rock Mech Min* 2005;42:521–530.
8. Nara Y, Kaneko K. Sub-critical crack growth in anisotropic rock. *Int J Rock Mech Min* 2006;43:437–453.
9. Fabre G, Pellet F. Creep and time-dependent damage in argillaceous rocks. *International Journal of Rock Mechanics and Mining Sciences* 2006;43(6):950–960.
10. Sterpi D, Gioda G. Visco-plastic behaviour around advancing tunnels in squeezing rock. *Rock Mech Rock Engng* 2009;42(2):319–339.
11. Yang W, Zhang Q, Li S, Wang S. Time-dependent behavior of diabase and a nonlinear creep model. *Rock Mechanics and Rock Engineering* 2014;47(4):1211–1224.
12. Zhou H, Yang Y, Gao H, Zhang C, Hu D. Experimental investigations on the short-and long-term behaviour of jinping marble in deep tunnels. *Eur J Environ Civ En* 2015;19(sup1):s83–s96.
13. Liu ZB, Shao JF. Strength behavior, creep failure and permeability change of a tight marble under triaxial compression. *Rock Mech Rock Eng* 2017;50(3):529–541.
14. Zhao Y, Wang Y, Wang W, Wan W, Tang J. Modeling of non-linear rheological behavior of hard rock using triaxial rheological experiment. *Int J Rock Mech Min Sci* 2017;93:66–75.
15. Zhao LY, Zhu QZ, Xu WY, Dai F, Shao JF. A unified micromechanics-based damage model for instantaneous and time-dependent behaviors of brittle rocks. *International Journal of Rock Mechanics and Mining Sciences* 2016;87:187–196.
16. Shi GC, Yang XJ, Yu HC, Zhu C. Acoustic emission characteristics of creep fracture evolution in double-fracture fine sandstone under uniaxial compression. *Engineering Fracture Mechanics* 2019;210:13–28.
17. Hu K, Shao JF, Zhu QZ, Zhao LY, Wang W, Wang RB. A micro-mechanics-based elastoplastic friction-damage model for brittle rocks and its application in deformation analysis of the left bank slope of jinping i hydropower station. *Acta Geotech* 2020;:3443–3460.
18. Dramis F, Farabollini P, Gentili B, Pambianchi G. Neotectonics and large-scale gravitational phenomena in the umbria–marche apennines, italy. In: *Seismically Induced Ground Ruptures and Large Scale Mass Movements. Field Excursion and Meeting 21–27 September 2001*; vol. 4. 2002:17–30.
19. Morelli S, Pazzi V, Frodella W, Fanti R. Kinematic reconstruction of a deep-seated gravitational slope deformation by geomorphic analyses. *Geosciences* 2018;8(1):26.
20. Tavenas F, Leroueil S. Creep and failure of slopes in clays. *Can Geotech J* 1981;18(1):106–120.
21. Intrieri E, Carlà T, Gigli G. Forecasting the time of failure of landslides at slope-scale: A literature review. *Earth-science reviews* 2019;193:333–349.
22. Yashima A. Slope failure at tunnel entrance due to excavation and its countermeasure, modern tunneling science and technology. *IS-KYOTO2001* 2001;:557–562.
23. Zhang F, Yashima A, Nakai T, Ye GL, Aung H. An elasto-viscoplastic model for soft sedimentary rock based on tij concept and subloading yield surface. *Soils Found* 2005;45(1):65–73.
24. Ling H, Ling H, Li L. Centrifuge modeling of slope failure induced by rainfall. In: *EGU General Assembly Conference Abstracts*; vol. 11. 2009:6730.
25. Irfan M, Uchimura T, Chen Y. Effects of soil deformation and saturation on elastic wave velocities in relation to prediction of rain-induced landslides. *Eng Geol* 2017;230:84–94.
26. Eker R, Aydın A. Long-term retrospective investigation of a large, deep-seated, and slow-moving

landslide using insar time series, historical aerial photographs, and uav data: The case of devrek landslide (nw turkey). *Catena* 2021;196:104895.
27. Rahimi A, Rahardjo H, Leong EC. Effect of antecedent rainfall patterns on rainfall-induced slope failure. *J Geotech Geoenviron* 2011;137(5):483–491.
28. Ren F, Ma G, Wang Y, Fan L. Pipe network model for unconfined seepage analysis in fractured rock masses. *Int J Rock Mech Min* 2016;88:183–196.
29. Gao Y, Yin Y, Li B, Feng Z, Wang W, Zhang N, Xing A. Characteristics and numerical runout modeling of the heavy rainfall-induced catastrophic landslide–debris flow at sanxicun, dujiangyan, china, following the wenchuan ms 8.0 earthquake. *Landslides* 2017;14(4):1361–1374.
30. Wang L, Yin Y, Zhang Z, Huang B, Wei Y, Zhao P, Hu M. Stability analysis of the xinlu village landslide (chongqing, china) and the influence of rainfall. *Landslides* 2019;16(10):1993–2004.
31. Zhang H, Li L. Modeling inclusion problems in viscoelastic materials with the extended finite element method. *Finite Elem Anal Des* 2009;45(10):721–729.
32. Zhang H, Rong G, Li L. Numerical study on deformations in a cracked viscoelastic body with the extended finite element method. *Eng Anal Bound Elem* 2010;34(6):619–624.
33. Sukumar N, Chopp DL, Béchet E, Moës N. Three-dimensional non-planar crack growth by a coupled extended finite element and fast marching method. *Int J Numer Methods Eng* 2008;76(5):727–748.
34. Wu W. Recent advances in modeling landslides and debris flows. Springer; 2015.
35. Lisjak A, Grasselli G. A review of discrete modeling techniques for fracturing processes in discontinuous rock masses. *J Rock Mech Geotech Eng* 2014;6(4):301–314.
36. Li W, Han Y, Wang T, Ma J. Dem micromechanical modeling and laboratory experiment on creep behavior of salt rock. *J Nat Gas Sci Eng* 2017;46:38–46.
37. Zhou S, Zhuang X, Rabczuk T. Phase-field modeling of fluid-driven dynamic cracking in porous media. *Comput Methods Appl Mech Engrg* 2019;350:169–198.
38. Ambati M, Gerasimov T, De Lorenzis L. A review on phase-field models of brittle fracture and a new fast hybrid formulation. *Comput Mech* 2015;55(2):383–405.
39. Francfort GA, Marigo JJ. Revisiting brittle fracture as an energy minimization problem. *J Mech Phys Solids* 1998;46(8):1319–1342.
40. Miehe C, Hofacker M, Welschinger F. A phase field model for rate-independent crack propagation: Robust algorithmic implementation based on operator splits. *Comput Method Appl M* 2010;199(45-48):2765–2778.
41. Borden MJ, Verhoosel CV, Scott MA, Hughes TJ, Landis CM. A phase-field description of dynamic brittle fracture. *Comput Method Appl M* 2012;217:77–95.
42. Mumford D, Shah J. Optimal approximations by piecewise smooth functions and associated variational problems. *Communications on pure and applied mathematics* 1989;42(5):577–685.
43. Ambrosio L, Tortorelli VM. Approximation of functional depending on jumps by elliptic functional via t-convergence. *Comm Pure Appl Math* 1990;43(8):999–1036.
44. Bourdin B, Francfort GA, Marigo JJ. Numerical experiments in revisited brittle fracture. *J Mech Phys Solids* 2000;48(4):797–826.
45. Wu JY, Nguyen VP, Nguyen CT, Sutula D, Bordas S, Sinaie S. Phase field modeling of fracture. *Adv Appl Mech: Multi-Scale Theor Comput* 2018;52.
46. Zhang X, Sloan SW, Vignes C, Sheng D. A modification of the phase-field model for mixed mode crack propagation in rock-like materials. *Comput Method Appl M* 2017;322:123–136.
47. Fei F, Choo JH. A phase-field model of frictional shear fracture in geologic materials. *Comput Methods Appl Mech Engrg* 2020;369:113265.
48. Fei F, Choo JH. Double-phase-field formulation for mixed-mode fracture in rocks. *Comput Methods Appl Mech Engrg* 2021;376:113655.
49. Zhou SW, Zhuang XY, Rabczuk T. Phase field method for quasi-static hydro-fracture in porous media under stress boundary condition considering the effect of initial stress field. *Theor Appl Fract Mec* 2020;107:102523.
50. Yu Z, Shao JF, Vu MN, Armand G. Numerical study of thermo-hydro-mechanical responses of in situ

heating test with phase-field model. *Int J Rock Mech Min* 2021;138:104542.
51. Yu Z, Shao JF, Duveau G, Vu MN, Armand G. Numerical modeling of deformation and damage around underground excavation by phase-field method with hydromechanical coupling. *Comput Geotech* 2021;138:104369.
52. Areias P, Rabczuk T, Msekh M. Phase-field analysis of finite-strain plates and shells including element subdivision. *Comput Methods Appl Mech Engrg* 2016;312:322–350.
53. Ren H, Zhuang X, Anitescu C, Rabczuk T. An explicit phase field method for brittle dynamic fracture. *Comput Struct* 2019;217:45–56.
54. Goswami S, Anitescu C, Chakraborty S, Rabczuk T. Transfer learning enhanced physics informed neural network for phase-field modeling of fracture. *Theor Appl Fract Mech* 2020;106:102447.
55. Shen R, Waisman H, Guo L. Fracture of viscoelastic solids modeled with a modified phase field method. *Comput Method Appl M* 2019;346:862–890.
56. Nguyen TT, Yvonnet J, Zhu QZ, Bornert M, Chateau C. A phase field method to simulate crack nucleation and propagation in strongly heterogeneous materials from direct imaging of their microstructure. *Eng Fract Mech* 2015;139:18–39.
57. Choo J, Sun W. Coupled phase-field and plasticity modeling of geological materials: From brittle fracture to ductile flow. *Comput Method Appl M* 2018;330:1–32.
58. Kuhn C, Schluter A, Muller R. On degradation functions in phase field fracture models. *Comp Mater Sci* 2015;108:374–384.
59. Perzyna P. Fundamental problems in viscoplasticity. In: *Advances in applied mechanics*; vol. 9. Elsevier; 1966:243–377.
60. Debernardi D, Barla G. New viscoplastic model for design analysis of tunnels in squeezing conditions. *Rock Mech Rock Eng* 2009;42(2):259–288.
61. Bonini M, Debernardi D, Barla M, Barla G. The mechanical behaviour of clay shales and implications on the design of tunnels. *Rock Mech Rock Eng* 2009;42(2):361–388.
62. Cristescu N, Gioda G, et al. Visco-plastic behaviour of geomaterials. Springer; 1994.
63. Borden MJ, Hughes TJ, Landis CM, Anvari A, Lee IJ. A phase-field formulation for fracture in ductile materials: Finite deformation balance law derivation, plastic degradation, and stress triaxiality effects. *Comput Method Appl M* 2016;312:130–166.
64. Mánica M, Gens A, Vaunat J, Ruiz DF. A time-dependent anisotropic model for argillaceous rocks. application to an underground excavation in callovo-oxfordian claystone. *Comput Geotech* 2017;85:341–350.
65. Su K. Constitutive models for the meuse/haute-marne argillites–modex-rep, european commission–nuclear science and technology. *Contract n FIKW-CT2000-00029, Deliverable* 2003;:2–3.
66. Bourdin B, Francfort GA, Marigo JJ. The variational approach to fracture. *J Elast* 2008;91(1-3):5–148.
67. Miehe C, Welschinger F, Hofacker M. Thermodynamically consistent phase-field models of fracture: variational principles and multi-field fe implementations. *Int J Numer Meth Eng* 2010;83(10):1273–1311.
68. Griffith A, Gilman JJ. The phenomena of rupture and flow in solids. *Transactions of the ASM* 1968;61:855–906.
69. Hofacker M, Miehe C. A phase field model of dynamic fracture: Robust field updates for the analysis of complex crack patterns. *Int J Numer Meth Eng* 2013;93(3):276–301.
70. Loew PJ, Peters B, Beex LA. Rate-dependent phase-field damage modeling of rubber and its experimental parameter identification. *J Mech Phys Solids* 2019;127:266–294.
71. Mandal TK, Nguyen VP, Wu JY, Nguyen-Thanh C, de Vaucorbeil A. Fracture of thermo-elastic solids: Phase-field modeling and new results with an efficient monolithic solver. *Comput Method Appl M* 2021;376:113648.
72. Qi S, Wu F, Zhou Y, Song Y, Gong M. Influence of deep seated discontinuities on the left slope of jinping i hydropower station and its stability analysis. *Bull Eng Geol Environ* 2010;69(3):333–342.
73. Huang R, Lin F, Yan M. Deformation mechanism and stability evaluation for the left abutment slope of jinping i hydropower station. *Bull Eng Geol Environ* 2010;69(3):365–372.

74. Zhou C, Jiang Q, Wei W, Chen Y, Rong G. Safety monitoring and stability analysis of left bank high slope at jinping-i hydropower station. *Q J Eng Geol Hydroge* 2016;49(4):308–321.
75. Waza T, Kurita K, Mizutani H. The effect of water on the subcritical crack growth in silicate rocks. *Tectonophysics* 1980;67:25–34.
76. Nara Y, Morimoto K, Hiroyoshi N, Yoneda T, Kanedo K, Benson PM. Influence of relative humidity on fracture toughness of rock: Implications for subcritical crack growth. *Int J Solids Struct* 2012;49:2471–2481.
77. Xu H, Zhou Z, Xu J, Ren H, Nie M, Wang L, Zheng H, Yang J. Experimental study of weakening effect of high water head on weak rock masses from jinping i hydropower station. *Rock Mech Rock Eng* 2013;32(4):207–4.